

Saturn's C ring and Cassini division: Particle sizes from Cassini UVIS, VIMS, and RSS occultations

Richard G. Jerousek^{a,*}, Joshua E. Colwell^a, Matthew M. Hedman^b, Richard G. French^c,
Essam A. Marouf^d, Larry W. Esposito^e, Philip D. Nicholson^f

^a Department of Physics and Florida Space Institute, University of Central Florida, Orlando, FL 32816, United States of America

^b Department of Physics, Univ. of Idaho, Moscow, ID 83844, United States of America

^c Department of Astronomy, Wellesley College, Wellesley, MA 02481, United States of America

^d Department of Electrical Engineering, San Jose State University, San José, CA 95192-0080, United States of America

^e Laboratory for Atmospheric and Space Physics, Univ. of Colorado, Boulder, CO 80309, United States of America

^f Department of Astronomy, Cornell University, Ithaca, NY 14853, United States of America

A B S T R A C T

Saturn's C ring and Cassini Division share many morphological traits: both contain numerous opaque, sharp-edged ringlets and gaps, broader low optical depth "background" regions, larger-optical depth regions that rise abruptly from the background (known as the C ring's plateaus and the Cassini Division's triple band feature), and linear ramps in optical depth up to the abrupt inner edges of the B ring and A ring, respectively. Throughout the majority of both regions, the surface mass density of the rings is small enough that the Toomre critical wavelength (most unstable wavelength for gravitational collapse) is comparable in size to, or smaller than, the largest individual ring particles. Thus, self-gravity wakes do not form in these regions, unlike the A and B rings where the critical wavelength is tens of meters and the self-gravity wakes introduce strong dependence of the observed optical depth on viewing geometry. In the absence of self-gravity wakes, we model the ring particle size distribution with a simple power-law, where the number of particles per unit area of the rings in the size range $[a, a + da]$ is given by $n(a)da = Ca^{-q}da$ between a_{\min} and a_{\max} . We fit normal optical depths derived from the power-law size distribution parameters and the thin-layers ring model of Zebker et al. (1985) to the wavelength-dependent optical depth profiles obtained by 3 Cassini Instruments: UVIS at $\lambda = 0.15 \mu\text{m}$, VIMS at $\lambda = 2.9 \mu\text{m}$, and RSS Ka-band ($\lambda = 9.4 \text{ mm}$), X-band at ($\lambda = 3.4 \text{ cm}$), and S-band ($\lambda = 13.0 \text{ cm}$).

We find that the C ring is best characterized by five or more thin layers of particles with a mean power-law index of $q \sim 3.16$ in the C ring background and $q \sim 3.05$ in the C ring plateaus, in the rings. We find a minimum particle radius of $a_{\min} \sim 4.1 \text{ mm}$ in the background C ring and plateaus and $a_{\min} \sim 6 \text{ mm}$ in the plateaus. The cross-section-weighted effective particle radius determined using the excess variance of UVIS signal beyond Poisson counting statistics by Colwell et al. (2018) constrains the size of the largest particles in the rings. We find the largest particles contributing to the power-law size distribution, and thus to the optical depth, are $a_{\max} \sim 10\text{--}15 \text{ m}$ in the background C ring and $a_{\max} \sim 5\text{--}6 \text{ m}$ in the C ring plateaus. This substantial difference in the sizes of the largest ring particles together with the overall shallower power law index in the plateaus explains their optical depth difference relative to the background C ring. Additionally, Baillié et al. (2013) used UVIS stellar occultations to find a distribution of small-scale, low optical depth gaps in the plateaus. These regions, with radial widths of $<100 \text{ m}$ and dubbed "ghosts", also appear in Cassini ISS images (Tiscareno et al., 2019) as "streaky" texture with an azimuthal length scale of many km but widths near the pixel scale of the images ($<300 \text{ m}$). Baillié et al. (2013) proposed that the ghosts are propeller features (Tiscareno et al. 2006) like those found in the A ring, opened by particles or aggregates with Hill radii $<20 \text{ m}$ in radius. Best-fit values of a_{\max} confirm that particles between 5 and 20 m sparsely populate the C ring plateaus and do not contribute significantly to the measured normal optical depth, but their presence in smaller numbers could account for the "streaky" texture as azimuthally limited gaps or propellers in the plateaus and in the Cassini Division's triple band feature. In the background C ring and background Cassini Division, where a_{\max} is $\sim 12 \text{ m}$, these larger particles or aggregates are ubiquitous and do contribute significantly to the measured normal optical depth, but their abundance and closer spacing may disturb the formation of azimuthally limited gaps such as those seen in the C ring plateaus. In the Cassini Division background and ramp, we find a shallower power law index of $q \sim 3.0$, and in the triple band feature we find $q \sim 2.9$. We find a similar smallest particle size cutoff as in the C ring but larger largest particles in the Cassini Division ramp.

We constrain the particle densities by dividing the surface mass densities determined from the dispersion of spiral density waves by the total particle volume integrated over a square meter of the ring slab. We derive low bulk particle densities of $\rho \sim 0.1\text{--}0.3 \text{ g/cm}^3$ except in the central background C ring where we find $\rho \sim 0.9 \text{ g/cm}^3$. These low derived densities may be due to inter-particle spaces within 1–20 m particle aggregates that contribute to the measured optical depth and thus to the upper end of the size distribution. Our results are consistent with Zhang et al. (2017) who reported particles with porosities $>75\%$ made of water ice with up to 11% silicate contaminate in the central background C ring.

* Corresponding author.

E-mail address: richard.jerousek@ucf.edu (R.G. Jerousek).

URL: <https://www.physics.cos.ucf.edu> (R.G. Jerousek), <https://www.physics.cos.ucf.edu> (J.E. Colwell).

<https://doi.org/10.1016/j.icarus.2019.113565>

Received 18 July 2019; Received in revised form 8 November 2019; Accepted 18 November 2019

Available online 20 November 2019

0019-1035/© 2019 Elsevier Inc. All rights reserved.

1. Introduction

Particles in any collisionally evolved system such as Saturn's rings roughly follow a truncated power-law size distribution (Dohnanyi, 1969) where the number of particles per unit area of radius in the interval $[a, a + da]$ is given by

$$n(a)da = n_0 \left(\frac{a}{a_0}\right)^{-q} da; a_{\min} \leq a \leq a_{\max}. \quad (1)$$

The four parameters of the size distribution are the number of particles per unit area, n_0 , of reference radius a_0 (which is taken to be 10 cm in this paper), the power-law index q , and the minimum and maximum particle radii, a_{\min} and a_{\max} . Outside of the interval $[a_{\min}, a_{\max}]$ the particle count is assumed to be zero. Laboratory studies and numerical simulations (Dohnanyi, 1969; Fujiwara et al., 1978; Matsui et al., 1982) show that a power-law particle size distribution with power law index q between $\sim 2-4$ is consistent with collisional evolution, and Brilliantov et al. (2015) constrains the power law index in Saturn's rings further, to $2.75 \leq q \leq 3.5$. The parameters of this simple size distribution can be determined from optical depth measurements at multiple wavelengths (Marouf et al., 1983; Tyler et al., 1983; Zebker et al., 1985; French and Nicholson, 2000; Cuzzi et al., 2009). However, structures such as self-gravity wakes, which impose viewing geometry dependence on apparent normal optical depths, can complicate the determination of the power-law size parameters (Jerousek et al., 2016). The Toomre critical wavelength, or most unstable wavelength for gravitational collapse (Julian and Toomre, 1966), is proportional to the ring's surface mass density, σ , and inversely proportional to the square of the ring particles' epicyclic frequency, κ . Throughout the C ring and the Cassini Division excluding the triple band feature, the ring surface mass density is low enough ($1-10 \text{ g/cm}^2$, Colwell et al. (2009a, 2009b), Baillié et al. (2011), Hedman and Nicholson (2013), and Tiscareno et al. (2013a)) and the ring particles' epicyclic frequencies are large enough that the Toomre critical wavelength is at or below the sizes of the largest individual ring particles, and self-gravity wakes are not expected to form. We focus this study on these two regions, which also share many morphological characteristics.

Saturn's C ring, the innermost broad demarcated region of Saturn's main rings, spans radial distances of $\sim 74,250 \text{ km}-91,990 \text{ km}$ from Saturn's center and is largely dominated by two distinct optical depth morphologies, dubbed the background and the plateaus (see Colwell et al., 2009a, 2009b for an overview of C ring features). The background C ring has a peak geometric normal optical depth (optical depth as measured perpendicular to the ring plane) of $\tau \sim 0.1$ near $83,000 \text{ km}$ with a gradual decline to $\tau \sim 0.05$ near the inner and outer edges of the ring. The optical depth also undulates by about 20% from its mean value with a length scale of $\sim 1000 \text{ km}$. This undulation length scale is consistent with the evolution of a homogeneous ring due to ballistic transport instability (Latter et al., 2012).

Eleven plateaus, named for their appearance in optical depth profiles, are dispersed throughout the ring, with the most prominent in the outer C ring. Smaller regions of enhanced optical depth dubbed embedded ringlets (Colwell et al., 2009a, 2009b) may be part of a morphological continuum with the broader plateaus. While the optical depth at the center of each of the C ring plateaus is at least several times larger than the surrounding C ring, the plateaus' normal optical depths are usually largest at their edges, giving them characteristic U-shaped optical depth profiles. The plateau edges span a few kilometers with a slight ramp exterior to the plateaus' inner edges. The mechanisms that maintain the edges are not well-understood, though it seems likely that ballistic transport from extrinsic micrometeoroid flux plays a role in confining at least their inner edges (Estrada et al., 2015). Studies of the dispersion of spiral density waves in both the C ring background and in several of the plateaus (Hedman and Nicholson, 2013, 2014; Baillié et al., 2011) yield estimates of the local surface mass density of $1-10 \text{ g/}$

cm^2 in the background and $1-4.5 \text{ g/cm}^2$ in plateaus P5, P7, and P10. This implies that the large differences in optical depths between the two regions are due to differences in either the particle densities or the size distributions of the particles.

The outermost region of the C ring, spanning ring plane radii of $\sim 90,620 \text{ km}-91,990 \text{ km}$, consists of a gradual radial increase in optical depth from $\tau \sim 0.1$ to $\tau \sim 0.25$ before an abrupt jump in optical depth at the inner edge of the B ring. This region, dubbed the C ring ramp, shows the characteristic features of ballistic transport of ring material that drifts radially inward from the massive B ring (Estrada et al., 2015; Latter et al., 2012; Durisen et al., 1989; Durisen et al., 1992; Durisen et al., 1996). Prominent C ring features are shown on a plot of UVIS normal optical depth from the ingress occultation of α Arae rev 32 (α Arae32I)¹ in Fig. 1(a).

The Cassini Division, between the A and B rings, consists of a series of gaps and ringlets where, like the C ring background, normal optical depths are $\tau \sim 0.1$. The Cassini Division has its own plateau-like feature, referred to as the "triple band", where optical depths are larger than the background by a factor of several but with edges that are not as sharp as the C ring plateaus and a central peak that is also not observed in C ring plateaus. Also, unlike the C ring plateaus, the triple band feature shows the variation in measured normal optical depth with ring plane incidence angle, B , that is characteristic of self-gravity wakes seen in the A and B rings (Fig. 12). The variation in normal optical depth is most notable exterior to the triple band feature's central peak and is not discernable in the first peak. One explanation is that somewhere in the triple-band, the ring particles' ability to aggregate transitions, which could also account for the central peak in optical depth.

Exterior to the triple band is another gradual increase in optical depth spanning $\sim 1500 \text{ km}$ radially, called the Cassini Division ramp. Like the boundary between the C ring ramp and the inner edge of the B ring, exterior to the Cassini Division ramp there is an abrupt jump in optical depth marking the inner edge of the A ring. Tiscareno et al. (2013a) analyzed the dispersion of the Iapetus ($-1:0$) nodal bending wave and found that although there is abrupt change in optical depth, the surface mass density of the rings only gradually increases into the A ring, suggesting a transition in particle or aggregate size at the inner edge of the A ring. Aside from some spiral density waves driven by resonances with various moons, broadly, the C ring ramp and Cassini Division ramp are nearly identical in optical depth profiles and their morphology has been generally explained by ballistic transport (Durisen et al., 1992). Prominent Cassini Division features are shown on a plot of UVIS normal optical depth from the occultation of α Arae32I in Fig. 1(b).

Previous studies have attempted to constrain the sizes of particles in Saturn's rings through remote sensing. Historical reviews of ring particle size distribution studies can be found in Pollack (1975), Cuzzi (1995), Cuzzi et al. (1984), Cuzzi et al. (2009), Dones (1998), and Esposito et al. (1983). Here, we highlight a few more recent studies that provide some background on the salient features of our analysis as well as several studies of ring particle sizes from the Cassini mission.

Voyager 1 Radio Science System (RSS) measured coherent radio waves at 3.6 cm (X-band) and 13.0 cm (S-band) wavelengths which passed through Saturn's rings en route to Earth. Studies by Marouf and Tyler (1982), Marouf et al. (1983), Tyler et al. (1983), and Zebker et al. (1985) inverted the forward scattered Voyager S-band radio signal to determine the sizes of the largest particles in the rings and used the differential X-band – S-band optical depth, $\Delta\tau_{X-S}$, to constrain the power-law index, q . Since the size of the smallest ring particles was expected to be smaller than the smallest measured wavelength (X-band), these studies assumed a minimum particle radius of $a_{\min} = 1 \text{ mm}$, well within

¹ Rev. numbers are used to identify the orbit or revolution of the Cassini spacecraft around Saturn during which the observation was made. Occultations are further identified by ingress (I) and egress (E) to indicate whether the occultation track was moving toward or away from Saturn, respectively.

the Rayleigh regime for both S-band and X-band radiation. Marouf et al. (1983) and Zebker et al. (1985) found $q \sim 3.11$ averaged over the central background C ring and $q \sim 3.05$ averaged over the C ring ramp ($\sim 90,500$ km – $91,990$ km) with a maximum particle size of $a_{\max} \sim 4\text{--}5$ m in both regions. Zebker et al. (1985) attempted to remove the discontinuity between the size distribution of particles larger than ~ 1 m (determined by the direct inversion of the forward-scattered S-band signal) with that of particles smaller than ~ 1 m (due to the assumed differential power-law with power-law index constrained by the differential X-band – S-band optical depth). They assumed that the discontinuity arose from the assumption that the rings are many particles thick and that only single-particle scattering contributed to the measured signal. By including an additional free parameter, N , representing the number of ring particle monolayers between which multiple-particle scattering can occur. They found that much of the C ring is better fit to a model consisting of one to several thin layers than a many-particle thick cloud. More recent studies of spiral density wave dispersion in the C ring and Cassini Division (Colwell et al., 2009a, 2009b; Baillié et al., 2011; Hedman and Nicholson, 2013, 2014) limit the scale height of the rings to <10 m in these regions, consistent with the view of Zebker et al. (1985).

French and Nicholson (2000) derived spatial profiles of the near-forward scattered signal in Earth-based observations of the occultation of 28 Sagittarii by Saturn's rings and together with data from the Voyager PPS (Photopolarimeter Subsystem) occultation of δ Scorpii constrained the parameters of the differential particle size distribution. They found $a_{\min} \sim 1$ cm, $a_{\max} \sim 10$ m, and $q \sim 3.1$ from the inversion of the forward-scattered stellar flux at $\lambda = 0.9, 2.1,$ and $3.9 \mu\text{m}$. French and Nicholson (2000) considered a many-particle-thick ring model and did not model multiple particle scattering. They stated that the inclusion of multiple

particle scattering would increase the size of the diffraction lobe and would lead to larger estimates of a_{\max} . The Earth-based observations of 28 Sagittarii also had limited sensitivity to particles smaller than ~ 1 cm since at Earth's distance from Saturn the diffraction lobe due to particles this size was larger than the aperture.

During a stellar occultation, the variance of the star signal in excess of that expected from Poisson counting statistics can be related to the average sizes of the ring particles' shadows. This method was applied to the Voyager PPS occultation data of δ Scorpii by Showalter and Nicholson (1990). They did not attempt to uniquely determine the four parameters of a differential power-law size distribution, but rather constrained the cross-section-weighted effective particle radius

$$a_{\text{eff}} = \sqrt{\frac{\int_{a_{\min}}^{a_{\max}} a^4 n(a) da}{\int_{a_{\min}}^{a_{\max}} a^2 n(a) da}} \quad (2)$$

Showalter and Nicholson (1990) found $a_{\text{eff}} \sim 1.2\text{--}2.4$ m in the background C ring and in the C ring ramp within $\sim 30\%$ of the value derived using the size distribution parameters determined by either Zebker et al. (1985) and French and Nicholson (2000). More recently, Colwell et al. (2018) applied this technique to the Cassini UVIS (Ultraviolet Imaging Spectrograph) occultation of β Centauri ($\beta\text{Cen}771$). They reported a_{eff} at 10-km radial resolution throughout Saturn's main rings and found that a_{eff} in the C ring plateaus and triple band feature of the Cassini Division is consistently smaller than in the background C ring or background Cassini Division by a factor of ~ 2 . For $q \sim 3$, a_{\max} is generally about 4–5 times a_{eff} . This suggests smaller largest particles in the plateaus and in the triple band feature than in the surrounding

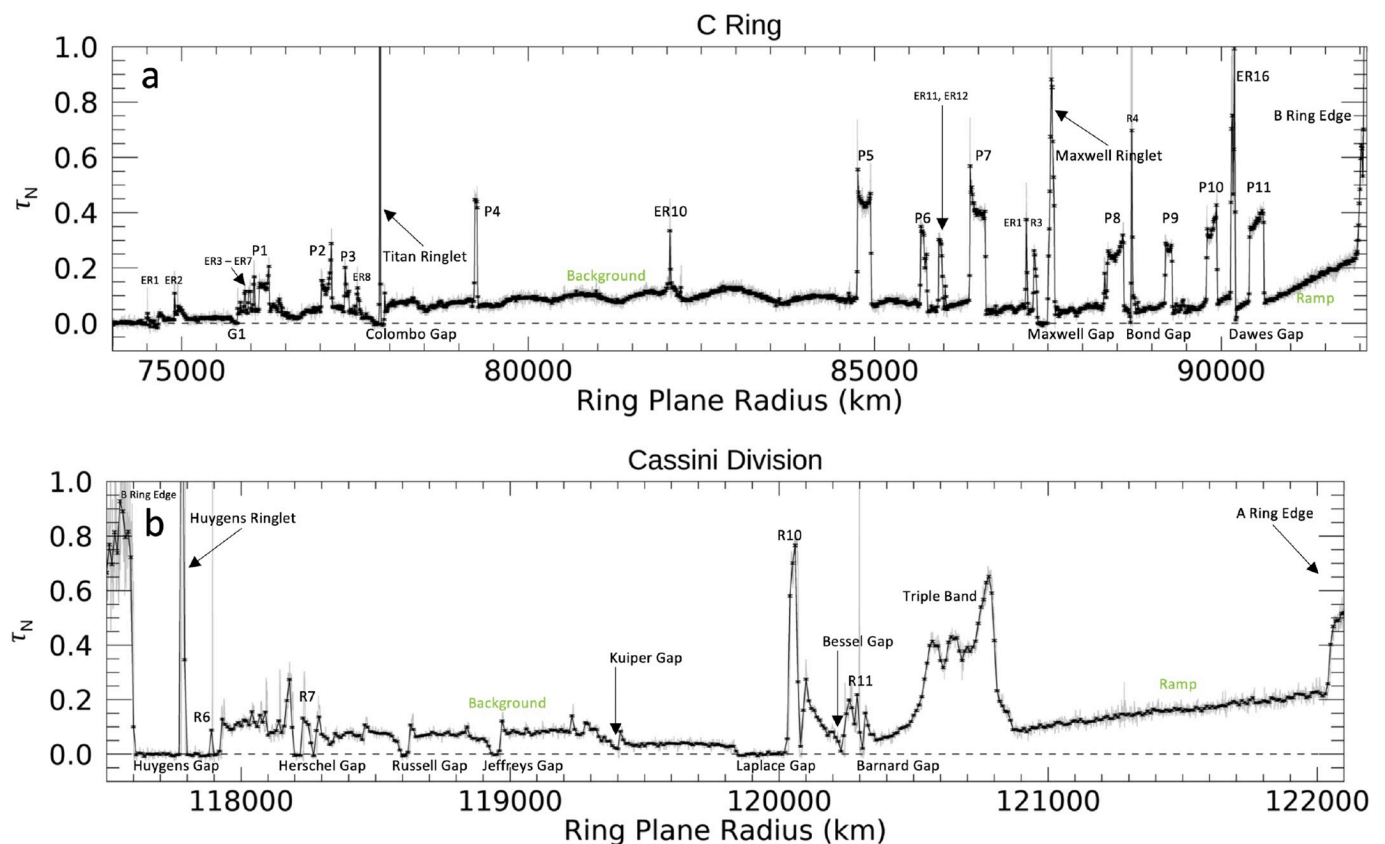


Fig. 1. Prominent ring features.

(a) The C ring and (b) Cassini Division optical depths at 10 km radial resolution from the UVIS occultation of α Arae32I. 1- σ error bars are shown at 10 km radial resolution. 1 km radial resolution optical depths are shown in light grey. Embedded ringlets (ER) and ringlets (R) where the peak normal optical depth is small and/or the radial width is <10 km are not labeled.

background ring regions.

Cuzzi et al. (2009) compared Cassini S-band, X-band, and Ka-band reconstructed optical depths from the Cassini rev. (7) ingress radio occultation to those computed using a power-law size distribution and the thin-layers model of Zebker et al. (1985). They found that the smallest particles in the mid-C ring and C ring ramp are ~ 4 mm with $q \sim 3.2$ if $a_{\max} = 10$ m and the particles are arranged in 1–4 monolayers. Cuzzi et al. (2009) did not constrain the power law parameters in the Cassini Division since the free-space power at each wavelength had not yet been estimated in that ring region.

Harbison et al. (2013) used Cassini VIMS solar occultations to constrain the sizes of the smallest particles in the A and C rings. Harbison et al. (2013) found that between 1 and 4% of the direct solar flux at near-infrared wavelengths was scattered away from the solar disk on the VIMS detector. Harbison et al. (2013) modeled the fraction of scattered sunlight in each of VIMS 144 spatial pixels at multiple wavelengths. By combining their spatial diffraction model with $q = 3.1$ from (Zebker et al., 1985) and $a_{\max} \sim 10$ m, they found the smallest particles in the background C ring to be $a_{\min} = 4.1^{+3.8}_{-1.3}$ mm. They also suggested that in order to fit their data at $2.3 \mu\text{m}$, q between 2.95 and 3.5 required $0.3 \text{ cm} \leq a_{\min} \leq 1.0 \text{ cm}$. Considering forward scattered near-infrared sunlight collected within the VIMS field-of-view, their study was not sensitive to the largest particles in the rings, a_{\max} . In contrast to their work, which analyzed the 2-D spatial diffraction pattern acquired during solar occultations, our study uses VIMS stellar occultations wherein VIMS measures near-infrared starlight in only a single pixel albeit with a shorter integration time (Section 2.2).

In Section 2, we give an overview of UVIS, VIMS, and RSS occultation observations, we review the procedure we use to calibrate UVIS and VIMS optical depth profiles, and we describe the effects of diffraction on the measured normal optical depth at each wavelength. In Section 3, we describe the thin-layers multiple scattering model of Zebker et al. (1985). We discuss the excess variance of UVIS occultation observations above Poisson counting statistics (Colwell et al., 2018) and how this provides an additional constraint on the largest particles in the rings where periodic structure such as self-gravity wakes is not present. In Section 4, we present our best fitting particle size distribution parameters throughout the C ring and Cassini Division using the thin-layers model and discuss the effects of adding additional parameters to the power-law size distribution. In Section 5, we discuss the radial variation in size distribution parameters, particle size sorting between ring region, and compare surface mass densities to those measured by the dispersion of spiral waves.

2. Observations

To constrain the parameters of the particle size distribution, we combine occultations measured by three Cassini instruments at five wavelengths: UVIS at $\lambda = 0.15 \mu\text{m}$, VIMS at $\lambda = 2.92 \mu\text{m}$, and the Radio Science Subsystem (RSS) at Ka-band (0.94 cm), X-band (3.6 cm), and S-band ($\lambda = 13$ cm) wavelengths. Normal optical depth profiles for each occultation were binned to 80-km radial resolution for comparison with RSS optical depth profiles from Cuzzi et al. (2009). In this section, we provide some of the salient features of each of the three instruments. Details on these instruments can be found in Esposito et al. (2004, UVIS), Brown et al. (2004, VIMS) and Kliore et al. (2004, RSS).

2.1. The ultraviolet imaging spectrograph (UVIS)

The UVIS high speed photometer (HSP) collects UV light over a 6.0×6.0 mrad field of view with an integration period of 1, 2, 4, or 8 ms. The high temporal resolution of the UVIS HSP allowed it to acquire photometric data of stellar occultations with typical spatial sampling of 10 m in the radial dimension of the rings, although the Fresnel scale ($\sqrt{\lambda D}$) is typically ~ 20 m and depends on D , the distance of the

spacecraft from the occultation point in the rings, and there is smear due to the azimuthal motion of the star track as well as the particles' orbital motion. The UVIS HSP consists of a photomultiplier tube with a CsI cathode behind a MgF_2 lens amplified by a high voltage pulse amplifier/discriminator (Esposito et al., 2004). As a photomultiplier, the UVIS HSP "counts" photons. Thus, the 1-standard deviation error in the signal measured during a single integration of the HSP is determined from Poisson counting statistics and is equal to the square root of the mean (expected) signal. The work function of CsI reduces the liberation of electrons from the cathode by photons with $\lambda > 190$ nm and strongly attenuates the sunlight reflected from the rings and Saturn when observing occultations of stars by the rings. On the small λ side, the MgF_2 lens also acts as a wavelength filter and strongly attenuates the spectrum for wavelengths less than ~ 115 nm. In this work, we consider the effective measured wavelength to be ~ 150 nm. A more rigorous approach would be to convolve the blackbody spectrum of the occulted star with the UVIS HSP's spectral response function. However, the variation in the peak wavelength in the blackbody spectrum over the range of stars observed by UVIS is small, and our analysis is not strongly sensitive to the effective measured wavelength. The UVIS data for the 288 occultations used in our study are available on the Planetary Data System (PDS) Ring-Moon Systems node. (Colwell et al., 2019)

2.2. The visual and infrared mapping spectrometer (VIMS)

The VIMS instrument can operate in several different modes. In occultation mode, VIMS acts as a high-resolution photometer collecting infrared light over a series of spectral channels with a wavelength range from 0.8–5.1 μm . For ring occultations, the 8 spectral channels covering the range from 2.87–3.0 μm are summed. These channels were chosen for their proximity to the strong water ice absorption feature to reduce the background signal from ring shine. Photon counts are converted to data number by an onboard analog to digital converter, and thermal background is removed. Unlike UVIS, the one standard deviation error in data number is dominated by read noise and detector dark current and is independent of the mean occultation signal level. Since 8 spectral channels are summed, the one standard deviation error in data number is $\sigma = \sqrt{8}$, thus the signal to noise ratio for VIMS is typically much higher than for UVIS. VIMS occultation data have a ring plane resolution of < 1 km but are binned to 10 km radial resolution for comparison with occultations from the other instruments. In occultation mode, VIMS collects light over a single spatial pixel with angular dimensions of 0.25×0.5 mrad, smaller than the (6.0×6.0 mrad) FOV of the UVIS HSP. In occultation mode, the star must be centered in the pixel prior to the ring occultation. Due to misalignment of the star within the pixel, some occultations exhibit a variation in signal strength when there is no intervening ring material. VIMS occultation data for 164 ingress and egress profiles are available on the Planetary Data System (PDS) Ring-Moon Systems node (Hedman and Nicholson, 2019). Those occultations where the systematic variation in data number (DN) is $> 2\%$ are flagged and were not included in our study.

2.3. The radio science subsystem (RSS)

During the first half of the Cassini mission, the radio science subsystem produced coherent radiation at wavelengths of 0.94 cm (Ka-band), 3.6 cm (X-band), and 13.0 cm (S-band) using an ultrastable quartz oscillator (Kliore et al., 2004). These coherent radio beams passed through Saturn's rings en route to Earth. The phase coherence of these signals allowed for reconstruction of normal optical depth profiles of the intervening rings from the diffraction-limited amplitude and phase (to remove the diffraction effects) of the signal received by one of NASA's Deep Space Network's 70 m or 34 m radio telescopes. X-band and Ka-band signals were received by the 70 m radio telescopes, which have the highest sensitivity and thus provide the most accurate radio

optical depth profiles. Simultaneously, X-band and S-band signals were measured by the 34 m radio receivers with lower signal to noise. The diffraction-corrected normal optical depth profiles have a resolution as high as 100 m in the ring plane (Marouf et al., 1986).

29 RSS optical depth profiles at 10 km and 1 km radial resolution measured simultaneously at X-band, S-band, and Ka-band are archived on the PDS (Planetary Data System) Ring-Moon Systems (Marouf, 2019). These profiles were measured before the failure of Cassini's ultrastable quartz oscillator in late 2011 and span ring opening angles from $B \sim 6^\circ$ to $B \sim 23.5^\circ$. Like VIMS and UVIS observations, some RSS occultations cut a chord across the rings and sample the same radial location at two different azimuths. These are divided into egress and ingress radial profiles giving a total of 50 ingress and egress RSS profiles of Saturn's main rings. Like with UVIS and VIMS observations, accurately estimating the free-space signal level complicates the accurate determination of normal optical depth profiles. Marouf (2019) measured the free-space power in the sufficiently clear regions exterior to Saturn's A ring and between Saturn's ionosphere and C ring as well as sufficiently wide gaps in the rings such as the Encke gap and Huygens gap. The free-space power in regions where rings are present is then estimated by least-squares polynomial fitting of the measured free space signal. In some cases, this process introduces a systematic error as large as $\sim 10\%$ in measured optical depth. Since X-band optical depth profiles were determined independently from data received by both the 70 m and 34 m DSN radio telescopes we compare these X-band profiles and exclude those with a systematic offset of larger than 5% from our study. We include 16 multi-wavelength RSS occultations of the rings.

2.4. Normal optical depth profiles

Normal optical depths, τ_N , from stellar occultations measured by UVIS and VIMS are determined using the method outlined in Colwell et al. (2010). The geometric optical depth measured along the line-of-sight path through the rings excludes the effects of diffraction and is given by

$$\tau = -\ln(T), \quad (3)$$

where the transparency, T , given by

$$T = \frac{I(t) - b}{I_0}, \quad (4)$$

is determined by subtracting a modeled background signal profile, b , from the measured signal, $I(t)$, and dividing by a model profile of the unocculted star signal, I_0 . I_0 is interpolated between gaps in the rings where there is a direct measurement of $I_0 + b$. For UVIS, the background signal is primarily due to reflected sunlight and Saturnshine off the ring particles and Lyman α emission from interplanetary hydrogen. It can be measured directly in the opaque regions of the B ring. We treat the background profile to be constant across the rings, although it likely increases at smaller Saturncentric distances due to increased Saturnshine as well as Lyman α transmission through the tenuous C ring. Colwell et al. (2006) estimated the variation in b from UVIS FUV data off of the star spot in the rings during several stellar occultations. In their analysis, the fractional difference in b between the C ring and central B ring (B3) was about the same as the fractional difference in b between the Cassini Division and central B ring and was $\sim 50\%$. For the occultations used in this study, I_0/b is between 10^2 and 10^5 . Therefore, in regions where $\tau \lesssim 1$, systematic errors in b could at most account for a few tenths of a percent difference in measured signal. The normal optical depth correction of the slant-path optical depth, μ , is the sine of the ring plane inclination angle, B , which is the declination of the star relative to Saturn's ring plane. The normal optical depth is then

$$\tau_N = \mu \ln \left(\frac{I_0}{I(t) - b} \right) \leq \tau_{\max}, \quad (5)$$

where the maximum measurable normal optical depth, τ_{\max} , corresponds to a signal within 1 standard deviation of zero. For UVIS occultations, the 1 standard deviation error in signal is the square-root of the mean signal due to Poisson photon counting statistics, and if the signal, $I(t)$ is binned with n samples per bin, both the error and the signal-to-noise ratio are larger by a factor of \sqrt{n} . Thus, if the UVIS signal is I , the 1-standard deviation error or minimum signal which would be statistically distinguishable from zero is \sqrt{b} and the maximum measurable optical depth that is distinguishable from infinity is

$$\tau_{\max} = \mu \ln \left(\frac{I_0}{\sqrt{b}} \right) \quad (6)$$

The 1- σ upper and lower errors in UVIS optical depth due to Poisson counting statistics are given by

$$\tau_{\pm} = \mu \ln(I_0) - \mu \ln \left(I_0 e^{-\tau_N/\mu} \mp \sqrt{I_0 e^{-\tau_N/\mu} + b} \right) \quad (7)$$

(Colwell et al., 2010). For VIMS, a detector dark current was removed on board Cassini, and the data were summed over eight spectral channels to increase the signal-to-noise ratio. One VIMS DN corresponds to ~ 300 IR photons, but the error in DN is independent of the signal level. For VIMS, the error in DN is $\sim \sqrt{8}$. If n measurements are summed in one bin, the 1- σ upper and lower errors in VIMS optical depth are given by

$$\tau_{\pm} = \mu \ln(I_0) - \mu \ln \left(I_0 e^{-\frac{\tau_N}{\mu}} \pm \sqrt{\frac{8}{n}} \right), \quad (8)$$

where I_0 is the mean DN of the unocculted star signal.

2.5. Particle size distribution effects on normal optical depth

For a many-particle-thick ring in which only single-particle scattering is considered, the classical normal optical depth measured by a detector with an infinitely narrow acceptance angle is determined by integrating over the cross-sectional areas of the particles in the size distribution:

$$\tau_N = \int_{a_{\min}}^{a_{\max}} Q_{\text{ext}}(a, \lambda) \pi a^2 n(a) da, \quad (9)$$

where $n(a)$ is the number of particles per square meter of the rings of radius a . Q_{ext} is the electromagnetic extinction efficiency of a ring particle of radius, a at wavelength, λ , and is determined from Mie theory. If $Q_{\text{ext}} = 1$, the normal optical depth is just the collective shadow size of the ring particles that block the incident electromagnetic radiation and τ_N is considered the geometric normal optical depth, τ_g . Babinet's principle states that a non-absorbing particle removes exactly as much light from the forward-directed beam through diffraction as is blocked by its cross-sectional area (e.g. Van de Hulst, 1957). Thus, for $a \gg \lambda$, Q_{ext} asymptotically approaches 2 when only the transmitted signal is measured.

Q_{ext} also asymptotically approaches 2 for RSS occultations even though the beam width for RSS radio occultations was not infinitely narrow. The Doppler shift of the forward-scattered signal away from the carrier frequency allows the attenuated directed radio flux to be determined. The RSS X-band, S-band, and Ka-band occultations included in our analysis have extinction efficiencies which are functions of size parameter, $x = 2\pi a/\lambda$. These were determined using a computational Mie model (Grainger et al., 2004). We assume particles are non-absorbing crystalline water ice at 100 K giving a complex index of refraction of $m = 1.78 + 0i$ (Dunn et al., 2002). Q_{ext} for X-band, S-band, and Ka-band radio wavelengths are shown as a function of particle radius, a , in Fig. 2. Particles with radii significantly smaller than the wavelength, λ contribute very little to the optical depth since they do not interact with the incident radiation. The ringing around the asymptotic value of $Q_{\text{ext}} = 2$ for large x follows from the solution of Maxwell's

equations at the boundary of spherical particles. The computation of $Q_{\text{ext}}(a, \lambda)$ is done in IDL using the Mie_Single.pro algorithm of Grainger et al. (2004). The computed extinction efficiencies for S, X, and Ka band wavelengths are shown in Fig. 2 as a function of scattering particle radius.

For UVIS and VIMS occultations, where the acceptance angle of the instrument's field of view (FOV) is not infinitely narrow, the measured optical depth is complicated by the fact that particles outside the direct line-of-sight to the star but within an angle $\theta_d \sim 1.22\lambda/2a$ will forward-scatter light into the FOV and add to the flux from the direct, attenuated star light. If the FOV is uniformly filled with particles that are large compared to λ , neighboring ring particles will replace all the light removed from the forward-directed beam by diffraction and $Q_{\text{ext}} = 1$. However, if there is a paucity of ring particles within an angular radius of θ_d of the line-of-sight to the star, Q_{ext} will depend on the fraction, f , of the circular diffraction lobe of angular radius θ_d that is (uniformly) filled with ring particles which have similar scattering properties (Cuzzi, 1985). Here we replace the angular dimensions of the rectangular FOV of each instrument ($L_{\text{VIMS}} = 0.25$ mrad, $W_{\text{VIMS}} = 0.50$ mrad, $L_{\text{UVIS}} = 6.00$ mrad, $W_{\text{UVIS}} = 6.00$ mrad) with the angular radius of an effective circular FOV:

$$\theta_{\text{ap}} = \sqrt{\frac{L \times W}{\pi}}. \quad (10)$$

For UVIS, $\theta_{\text{ap}} \sim 3.50$ mrad and for VIMS, $\theta_{\text{ap}} \sim 0.20$ mrad. The critical particle radius below which diffraction effects become important is $a_{\text{crit}} = 1.22\lambda/2\theta_{\text{ap}} \sim 8.86$ mm for VIMS and ~ 27 μm for UVIS. Thus, if the FOVs of both instruments are uniformly filled by particles of radius $a = 1$ mm (large compared with both wavelengths), a larger fraction of infrared star light will be scattered out of the small VIMS FOV (that will not be replaced by neighboring ring particles) than the fraction of ultraviolet star light that is scattered out of the larger UVIS FOV because of the differences in both the measured wavelength and the angular radius of the aperture. Particles of radius $a = 1$ mm produce a circular diffraction lobe of angular radius $\theta_d = 1.22\lambda/2a \sim 0.09$ mrad for UVIS.

For UVIS with its wide FOV and small measured wavelength, $\theta_d \ll \theta_{\text{ap}}$, the effective extinction efficiency for UVIS is given by:

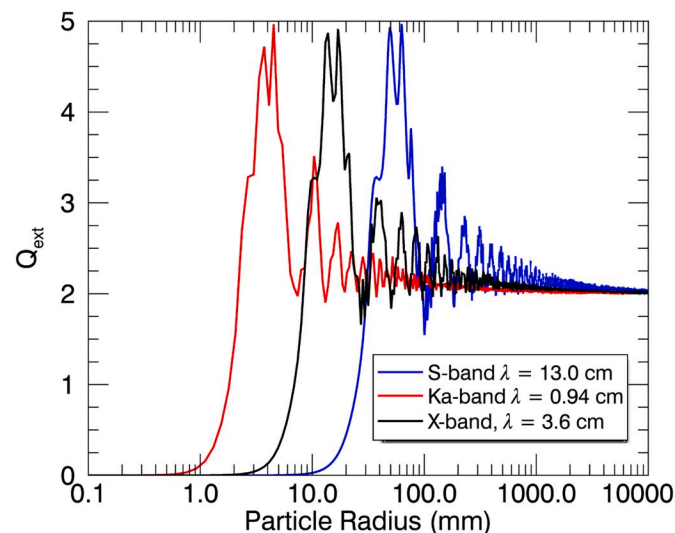


Fig. 2. The Mie-model extinction efficiencies for S, X, and Ka band wavelengths. Q_{ext} is shown as a function of scattering particle radius. In the geometric limit ($ka \gg 1$), the extinction efficiency oscillates around 2 due to Babinet's principle: large particles remove twice the radiation from the direct beam as their geometric cross-section blocks. In the Rayleigh regime ($ka \ll 1$) the extinction efficiency and therefore the contribution of these particles to the normal optical depth goes to zero: these particles are essentially invisible to the long-wavelength light.

$$Q_{\text{UVIS}} = 2 - f, \quad (11)$$

assuming there are few particles smaller than 26 μm contributing to the optical depth. With rare exceptions, such as R9 located in the Laplace Gap of the Cassini Division which consists of 10–100 μm particles (Hedman et al., 2010), this assumption is corroborated throughout Saturn's main rings by differential optical depth measurements at micron wavelengths, ring phase-function analysis, and microwave emissivity measurements (Dones et al., 1993; French and Nicholson, 2000; Spilker et al., 2005).

f depends on the distance over which the ring is uniform in its scattering properties as well as θ_d which depends on the sizes of the ring particles and the line-of-sight distance from the spacecraft to the rings (Harbison et al., 2013; Becker et al., 2015; Jerousek et al., 2016). UVIS occultation observations took place while Cassini was between 145,000 km and 3 million km from the rings with a mean line-of-sight distance of ~ 1 million km. At this distance, and if particles of radius ~ 1 mm are abundant, $f \sim 1$ unless the ring varies significantly over a radial scale of ~ 90 km, for example if the occultation point is within 90 km of a gap or ring edge.

For VIMS, 1 mm particles will produce a diffraction lobe of angular radius $\theta_d \sim 1.77$ mrad, so that $\theta_d \gg \theta_{\text{ap}}$. For VIMS occultations, the effective extinction efficiency is complicated by the presence of particles small enough to produce a diffraction lobe larger than $\theta_{\text{ap}} \sim 0.20$ mrad we have

$$Q_{\text{VIMS}} = 2 - H(a - a_{\text{crit}}) \cdot f \quad (12)$$

where $H(a - a_{\text{crit}})$ is the Heaviside step function centered on critical particle radius $a_{\text{crit}} \sim 8.86$ mm. A cartoon illustrating the dependence of the effective extinction efficiency, Q_{ext} , on f , a , λ , θ_{ap} , and θ_d is shown in Fig. 3 comparing VIMS and UVIS FOVs.

In order to estimate f , we assume the occulted star is centered in the instrument's effective circular FOV of angular radius given by Eq. (11). We assume that all regions where $\tau_g > 0.02$ are uniformly filled with 5 mm particles and that those regions where $\tau_g < 0.02$ have no particles. We calculate the fraction of a circular diffraction lobe centered on the ring occultation point and with a radius of $D\theta_d$ where there are particles, where D represents the line-of-sight distance from Cassini to the ring occultation point. For example, when the VIMS occultation of RCass651 crosses a ring radius of 119,000 km, Cassini is $D = 782,159$ km from the occultation point in the rings. For 5 mm radius particles, $\theta_d = 1.22\lambda/2a \sim 0.35$ mrad and the radius of the diffraction lobe projected into the rings is ~ 138 km. This region of the rings includes the Jeffries gap which is ~ 35 km across and 38.6 km inward of the center of diffraction lobe. Thus, f is the fraction of the circular diffraction lobe that is uniformly filled with particles, which in this case is approximately the fractional area of the diffraction lobe that is outside of the Jeffries gap, and $f \sim 0.93$. Fig. 3 depicts f as the yellow diffraction lobe centered on the star. As the occultation point approached the outer edge of the A ring, the circular diffraction lobe of angular radius θ_d shown as the yellow surrounding the star is only half filled with ring material and $f \sim 0.5$.

3. Model

3.1. The thin-layers ring model

Zebker et al. (1985) modeled rings as a small number (N) of thin, parallel particle layers. In this model, multiple scattering of the incident radiation can only occur between successive particle layers. Zebker et al. (1985) were motivated by the discrepancy between the particle size distribution for particles of radius > 1 m determined from the direct inversion of the forward-scattered S-band Voyager signal and the power-law size distribution inferred from differential X-S band optical depths for particles of radius < 1 m. They estimated the wavelength-dependent normal optical depth of the model by assuming multiple scattering only

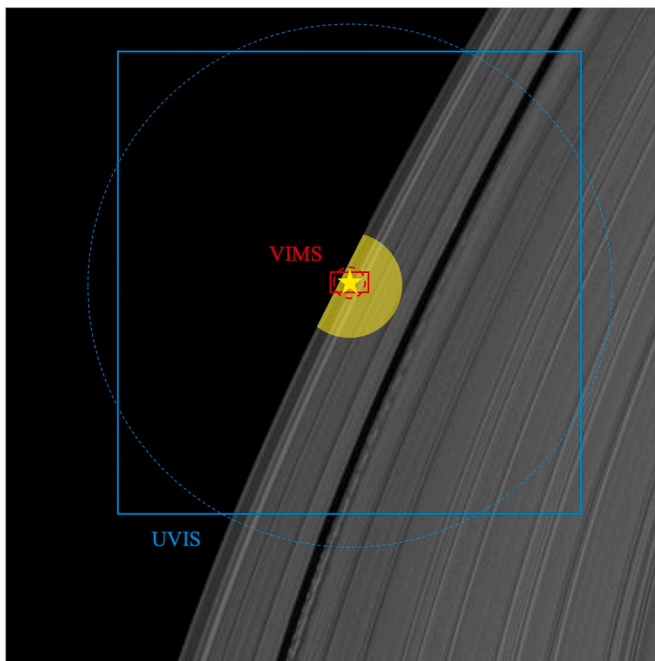


Fig. 3. VIMS and UVIS FOV's. The rectangular pixel of angular dimensions 0.25×0.5 mrad of the VIMS instrument (red) and the square UVIS field of view of angular dimensions 6.0×6.0 mrad (blue). During stellar occultations, $2.9 \mu\text{m}$ light diffracted out of the VIMS pixel is not replaced by light diffracted by neighboring particles. The much larger field of view and smaller effective wavelength of the UVIS HSP ($0.15 \mu\text{m}$) place the entirety of the diffraction cone within the field of view for particles larger than $25 \mu\text{m}$ in radius. Still, Q_{UVIS} depends on the fraction, f of the circular diffraction lobe (yellow) which is uniformly filled with ring particles. Close to the A ring outer edge $f \sim 0.5$. The background image is the January 3rd, 2008 ingress occultation of the star Antares (α Scorpii) by the outer A ring (NASA/JPL-Caltech/Space Science Institute) captured by the narrow-angle camera from an angle of 34° above the ring plane at a distance of 541,000 km. The relative sizes of the VIMS and UVIS field of view (FOV) are accurate; however, the sizes of the two FOVs are not to scale with the background image at the distance of the spacecraft from the rings during the time the image was taken. (For interpretation of the references to colour in this figure legend, the reader is referred to the web version of this article.)

takes place between particles in successive particle layers and that the n -th order photon scattering event is Poisson distributed with optical depth. This model is especially useful in regions where $\tau \sim 1$ and/or normal optical depths are measured at small ring opening angles, B . Independent measurements by [Brahic and Sicardy \(1981\)](#), [Lane et al. \(1982\)](#), and [Jerousek et al. \(2011\)](#) of sharp-edged ringlets and at various other locations in the rings have shown that, at least near these edges, the rings are no more than tens of meters thick, comparable to several of the largest particle's diameters. Indirect measurements of the ring's scale height from self-gravity wake analysis by [Colwell et al. \(2006\)](#), [Esposito et al. \(2017\)](#) and [Tiscareno et al. \(2019\)](#) as well as derivations of the ring scale height from the dispersion of spiral density waves by [Baillié et al. \(2011\)](#), [Colwell et al., 2009a](#), [Tiscareno et al., 2008](#), and [Hedman and Nicholson \(2013, 2014\)](#) give ring thicknesses of ≤ 10 m.

Below we briefly summarize this derivation of the normal optical depth of a ring consisting of N particle monolayers, measured at wavelength λ . For more details see [Zebker et al. \(1985\)](#) and [Cuzzi et al. \(2009\)](#).

We begin by deriving the near-forward signal relative to the free space power per unit area after a single particle scattering event as:

$$\frac{I_1}{I_0} = \frac{e^{-\frac{\tau}{\mu_0}}}{4\pi\mu_0} \int_{a_c}^{\infty} \left[\frac{2J_1(kas\sin\theta)}{\sin\theta} \right]^2 \pi a^2 n(a) da, \quad (13)$$

where k is the wavenumber ($2\pi/\lambda$), μ_0 is the sine of the angle between the wave vector of the incoming plane wave and the ring plane ($\sin|B|$), and J_1 is the first-order Bessel function of the first-kind. The lower-bound on the radii of particles effectively contributing to the scattered signal is a_c , with $ka_c \gg 1$. If optical depths are of order unity or higher, it is not appropriate to assume single scattering. However, the likelihood of a photon emerging in the direction of the detector decreases rapidly with the number of times, n , the photon is scattered by intervening ring particles. If multiple scattering between the ring particles occurs, the single-scattered component can be found by deconvolving the multiply-scattered signal, given in terms of the particle phase function, $\Phi(\theta)$ and the single-scattering albedo, ϖ_0 by [Cuzzi et al. \(2009\)](#):

$$\frac{I_s}{I_0} = \sum_{n=1}^{\infty} \frac{I_n(\theta, \lambda)}{I_0} = \sum_{n=1}^{\infty} \left[\frac{1}{n!} \left(\frac{\tau}{\mu_0} \right)^n e^{-\frac{\tau}{\mu_0}} \right] \left[\frac{\varpi_0 \Phi(\theta)}{4\pi} \right]^{*n}, \quad (14)$$

where the symbol *n denotes convolution of the term with itself n times. In the low normal optical depth limit, $\tau \ll 1$, single-particle scattering ($n = 1$) contributes the most to the near-forward scattered signal, and Eq. (14) becomes

$$\frac{I_s}{I_0} \approx \frac{\tau e^{-\frac{\tau}{\mu_0}}}{4\pi\mu_0} \varpi_0 \Phi(\theta) \quad (15)$$

Thus, when single-particle scattering dominates, $\varpi_0 \Phi(\theta)$ is defined in terms of the size distribution $n(a)$ by

$$\varpi_0 \Phi(\theta) \approx \frac{\int_{a_c}^{\infty} \left[\frac{2J_1(kas\sin\theta)}{\sin\theta} \right]^2 \pi a^2 n(a) da}{\int_0^{\infty} Q_{\text{ext}}(a, \lambda) \pi a^2 n(a) da}. \quad (16)$$

Interpreting the terms in the infinite series of Eq. (14) as a sum of probabilistic events, the n -th order scattering is Poisson distributed in slant-path optical depth (τ/μ_0 , optical depth measured along the line-of-sight through the rings) with the probability of scattering given by ϖ_0 and with the scattered energy emerging in the direction θ with probability density $\Phi(\theta)/4\pi$. Though multiple scattering includes an infinite number of interactions, the probability that energy emerges in the direction of the detector decreases rapidly with $n > \tau/\mu_0$.

If the number of scattering events is limited by the small vertical extent of the ring, the Poisson distribution can be replaced with a binomial distribution over a parameter, p , which represents the probability of a single interaction between the incident radiation and a ring particle. For a model with N layers, Eq. (14) becomes

$$\frac{I_s}{I_0} = \sum_{n=1}^N \left[\binom{N}{n} p^n (1-p)^{N-n} \right] \left[\frac{\varpi_0 \Phi(\theta)}{4\pi} \right]^{*n}. \quad (17)$$

The probability of the incident light emerging with no interactions is $(1-p)^N \sim \exp(-\tau/\mu_0)$. Hence, p must be given by

$$p = \left(1 - e^{-\frac{\tau}{\mu_0 N}} \right), \quad (18)$$

and the optical depth after N interactions of the incoming radiation with ring particle monolayers is

$$\tau(\lambda) = -2\mu_0 N \ln \left[1 - \frac{1}{2\mu_0 N} \int_{a_{\min}}^{a_{\max}} Q_{\text{ext}}(a, \lambda) \pi a^2 n_0 \left(\frac{a}{a_0} \right)^{-q} da \right] \quad (19)$$

It should be noted that the classical optical depth of a many-particle-thick ring, considering only single-particle scattering (Eq. (10)) is recovered from the thin-layers model in the limit that N goes to infinity. It should also be noted that N is more representative of the number of scattering events that contribute significantly to the forward-scattered signal and not necessarily to the number of particle layers in the rings since particle sizes vary larger scale than the wavelengths measured in

this study. A cartoon illustrating the thin-layers model is shown in Fig. 4. Since N is not a direct measure of particle layers, individual particles could be significantly larger than the spacing between layers.

We fit the measured normal optical depths to those computed using Eq. (19) over a wide range of the free parameters, a_{\min} , a_{\max} , n_0 , q , and N (the number of particle monolayers). The best-fit parameters are determined by minimizing the reduced chi-squared statistic

$$\chi^2 = \frac{1}{\nu} \sum_{i=0}^n \frac{(\tau_{\text{comp},i} - \tau_{\text{data},i})^2}{\sigma^2}, \quad (20)$$

where ν is the number of occultations fit at that radial location, n , minus the number of free parameters (five) minus one. Reducing χ^2 by the number of occultations and the number of free model parameters is necessary since all occultations do not cover the radial full extent of the rings, but it has the added benefit of allowing us to quantitatively compare the goodness of fit of models with different numbers of free parameters. In Eq. (20), the UVIS and VIMS variances, σ^2 , were determined by squaring one-half the difference between the upper and lower one-standard deviation errors in optical depth determined using Eqs. (7) and (8). RSS variances in optical depth were estimated by measuring the sample variance over a boxcar with a radial width of 10 points (100 km) and filtering out points where the optical depth deviates from the median significantly, such as the edges of embedded ringlets or plateaus.

3.2. Excess variance from UVIS occultations as an additional constraint

Differential optical depth measurements from wavelengths between $\lambda = 0.15 \mu\text{m}$ and $\lambda = 13 \text{ cm}$ are not sensitive probes of particles larger than 1 m in radius. However, high-resolution UVIS optical depth profiles contain information on the sizes of the largest ring particles in the excess variance of the occulted star's signal beyond that which is predicted by Poisson photon counting statistics (Showalter and Nicholson, 1990; Colwell et al., 2018). Colwell et al. (2018) normalized the excess variance in star signal, E , by dividing the variance of the occulted star's signal beyond the Poisson variance, (which is equal to the mean of the signal) by the square of the mean signal over the radial bin over which the variance was sampled. Using the occultation of $\beta\text{Centauri}77\text{I}$, Colwell et al. (2018) determined E at 10 km resolution throughout Saturn's main rings.

If E is solely due to the distribution of spherical particles' cross-sections within the integration area, A , and not due to holes such as ghosts (Baillié et al., 2013) or elongated particle aggregates such as the self-gravity wakes that dominate the structure of the A and B rings (Colwell et al., 2006, 2007, Hedman et al., 2007, Nicholson and Hedman (2010), Jerousek et al., 2016), then a_{eff} (see Eq. (2)) is as given by Showalter and Nicholson (1990):

$$a_{\text{eff}} = \sqrt{\frac{E\mu A}{\pi\tau e^{-2\tau}}}. \quad (21)$$

If q and a_{\min} are known or can be estimated, Eq. (2) can be inverted to give $a_{\max}(a_{\text{eff}})$. The inversion has no simple algebraic solution but can be solved iteratively. Using a_{eff} determined by Colwell et al. (2018) and assuming the excess variance in star signal is solely due to a distribution of spherical particles and not due to elongated aggregates such as self-gravity wakes, we can place an additional upper limit on a_{\max} . Colwell et al. (2018) assumed that the ring particles are much smaller than the area, A , of the rings over which light is collected during a single integration of the UVIS HSP (1 ms for the $\beta\text{Centauri}77\text{I}$ occultation). The dimensionless parameter $\delta = \pi a_{\text{eff}}^2 / \mu A$ is much less than ~ 0.1 throughout the C ring and Cassini Division except in the Cassini Division ramp, where $\delta \sim 0.1$. Thus, in the Cassini Division ramp, the assumption no longer holds that the particles are small compared to the area, A .

If the normalized excess variance, E , is also due to particle aggregates or holes, then a_{\max} for a given q and a_{\min} is smaller than that which would be derived assuming the excess variance is solely due to a distribution of spherical particles. Thus, a_{\max} determined by inverting Eq. (3) represents an upper limit on the radii of the largest particles. Fig. 5 shows a_{\max} versus a_{eff} for a range of values of a_{\min} and q . Our fitting routine uses a library of values of a_{\max} determined over a wide range of a_{\min} and q and computed using a_{eff} determined from the normalized excess variance from the $\beta\text{Centauri}$ (77) ingress occultation to limit the range of a_{\max} when fitting optical depths to the thin-layers model.

Essentially, fitting the multitude of VIMS, UVIS, and RSS occultations to the thin-layers model allows us to simultaneously constrain the five free model parameters: N , n_0 , a_{\min} , a_{\max} , q due to a variety of different aspects of the occultations: The cutoffs of the three RSS extinction efficiencies together with the VIMS cutoff at $a_{\text{crit}} = 8.86 \text{ mm}$, which affect the measured normal optical depth at each wavelength, predominately provide tight constraints on both a_{\min} and q . More indirectly, an upper

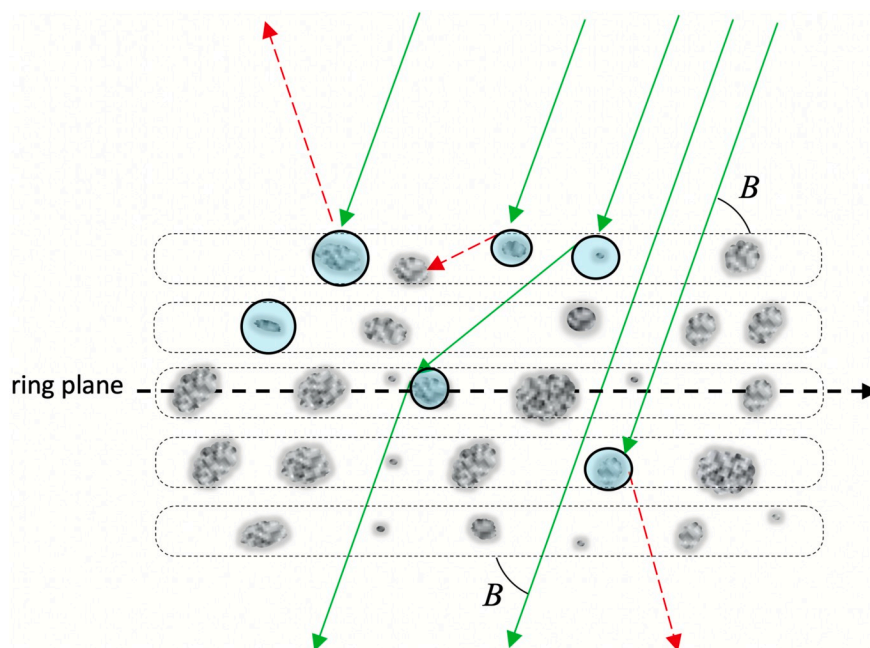


Fig. 4. The thin-layers model of Zebker et al. (1985). In the thin-layers model of Zebker et al. (1985), the ring particles are separated into monolayers. Radiation incident on the rings at angle B can be scattered from particles in adjacent layers, but not from particles within the same layer. This cartoon depicts a vertically oriented ring consisting of $N = 5$ thin layers. Emerging solid (green) rays represent forward scattered radiation collected by the receiver. Dashed (red) rays represent radiation which is scattered out of the receiver's FOV. The circles (blue) outlining selected ring particles represent these particles' electromagnetic cross-sections at wavelength, λ : $Q_{\text{ext}}(\lambda)\pi a^2$. (For interpretation of the references to colour in this figure legend, the reader is referred to the web version of this article.)

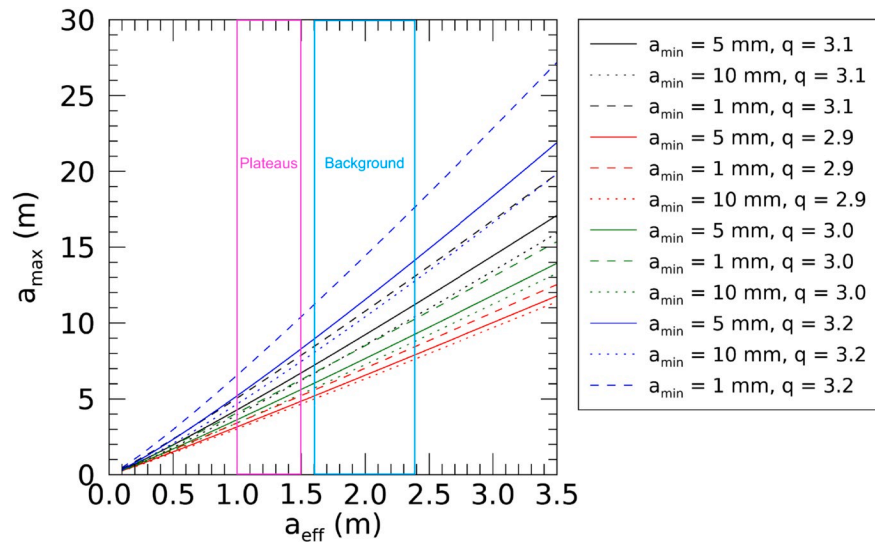


Fig. 5. a_{\max} vs. a_{eff} for a range of a_{\min} and q . The iterative solution of the inversion of Eq. (2) relates a_{\max} to a_{eff} determined by Colwell et al. (2018) and provides an additional constraint on the size distribution. In general, for $q \sim 3$, a_{\max} is 3–5 times larger than a_{eff} .

limit on a_{\max} is provided by the excess variance from the UVIS occultation ($\beta\text{Cen}771$) beyond Poisson counting statistics from Colwell et al. (2018). The number of scattering events, N is primarily constrained by the variation in optical depth with ring opening angle, B . And n_0 is most sensitive to the average optical depth at the occultation point. While these represent the parameters to which the individual model parameters are most sensitive, the minimization of χ^2 provides consistency between the individual optical depth integrals.

4. Results

4.1. The C ring

We fit 95 UVIS, 38 VIMS, and 16 (3 wavelength) RSS normal optical depth profiles to those computed using the thin-layers model of Zebker et al. (1985) by minimizing the reduced χ^2 statistic (Eq. (20)). The upper limit on a_{\max} is chosen from a library of values that simultaneously minimizes χ^2 and fits the value of a_{eff} determined by Colwell et al. (2018) from the occultation of $\beta\text{Centauri}771$. We fit occultations spanning ring

opening angles, B , from 3° to 70° to determine the best-fit model parameters over 10 km radial intervals. We exclude occultation points where $\tau \geq \tau_{\max}$, the maximum measurable optical depth (Eq. (6)). We also exclude ring regions where $\tau_{\text{UVIS}} \leq 0.02$ from our analysis because the relative uncertainty in the optical depth is large at these low optical depths. Throughout this section we discuss the mean values of the best-fitting parameters over each broad ring region. These values and their standard deviations over each region are summarized in Table 1. The best-fit parameters that minimize the reduced χ^2 are shown throughout the C at 10 km radial resolution in Fig. 6. Throughout the C ring, $\chi^2 \sim 1$ –5 (Fig. 6f) and is positively correlated with τ_N (Pearson correlation coefficient, $r = 0.71$).

In the background C ring, where $\tau_{\text{UVIS}} \lesssim 0.1$ and $\chi^2 \sim 1.2$, we find that the thin-layers model reproduces the wavelength-dependent measured optical depths (Fig. 7) to within a few to 10% with $N \sim 5$ (Fig. 6e) though in several 10-km radial intervals $N > 30$ was a better fit the measured optical depths. $N = 30$ is the maximum value we chose to display in Fig. 6e though the fitting routine's parameter space spans $N = 1$ –22,000 and some locations better fit larger N . $N \gtrsim 30$ indicates that the

Table 1
Mean best-fitting power-law parameters and their standard deviations over different ring regions.

| Region | τ | | n_0/τ_{vis} | | q | | a_{\min} (mm) | | a_{\max} (m) | | N | | χ^2 | |
|-----------------------|--------|------|-------------------------|------|------|------|-----------------|------|----------------|------|-----|------|----------|------|
| | M | SD | M | SD | M | SD | M | SD | M | SD | M | SD | M | SD |
| C ring | | | | | | | | | | | | | | |
| P1 | 0.14 | 0.01 | 36.0 | 1.1 | 3.05 | 0.02 | 4.27 | 0.13 | 5.4 | 0.7 | 5 | 1 | 1.36 | 0.16 |
| P2 | 0.14 | 0.03 | 35.0 | 1.6 | 3.06 | 0.03 | 4.29 | 0.15 | 5.4 | 0.6 | 5 | 1 | 1.46 | 0.36 |
| P3 | 0.12 | 0.02 | 36.1 | 1.6 | 3.05 | 0.04 | 4.12 | 0.37 | 5.6 | 0.2 | 6 | 1 | 1.37 | 0.11 |
| P4 | 0.44 | 0.01 | 27.5 | 3.0 | 3.12 | 0.02 | 5.65 | 1.37 | 10.3 | 2.0 | 8 | 1 | 3.39 | 0.56 |
| Background C ring | 0.05 | 0.03 | 36.0 | 5.3 | 3.16 | 0.08 | 4.15 | 0.72 | 11.0 | 1.8 | 5 | 2 | 1.20 | 0.63 |
| P5 | 0.43 | 0.01 | 33.9 | 2.0 | 3.01 | 0.01 | 6.56 | 0.27 | 6.3 | 0.4 | 24 | 9 | 2.99 | 0.32 |
| P6 | 0.33 | 0.01 | 30.0 | 6.1 | 3.21 | 0.06 | 5.98 | 0.60 | 12.5 | 1.5 | 15 | 8 | 2.96 | 0.45 |
| P7 | 0.40 | 0.01 | 34.4 | 2.5 | 3.04 | 0.01 | 4.04 | 1.29 | 6.3 | 0.9 | 9 | 4 | 2.98 | 0.16 |
| P8 | 0.25 | 0.02 | 37.0 | 1.2 | 3.09 | 0.01 | 4.89 | 0.43 | 6.3 | 0.2 | 12 | 7 | 1.69 | 0.25 |
| P9 | 0.27 | 0.01 | 33.1 | 1.1 | 3.09 | 0.02 | 5.58 | 0.15 | 5.3 | 0.45 | 7 | 1 | 2.62 | 0.20 |
| P10 | 0.32 | 0.01 | 29.2 | 2.7 | 3.17 | 0.10 | 3.62 | 0.58 | 7.7 | 0.5 | 9 | 2 | 2.10 | 0.26 |
| P11 | 0.37 | 0.02 | 36.0 | 4.7 | 3.00 | 0.03 | 6.09 | 1.92 | 5.7 | 0.9 | 15 | 8 | 2.51 | 0.42 |
| C ring ramp | 0.15 | 0.05 | 30.3 | 2.5 | 3.16 | 0.02 | 3.83 | 0.25 | 13.1 | 1.5 | 6 | 4 | 1.53 | 0.25 |
| Cassini division | | | | | | | | | | | | | | |
| Background cass. div. | 0.07 | 0.02 | 39.5 | 4.2 | 3.01 | 0.04 | 4.11 | 0.45 | 8.9 | 1.6 | 6 | 2 | 1.15 | 0.27 |
| Triple band | 0.43 | 0.09 | 32.1 | 5.1 | 2.94 | 0.02 | 6.05 | 1.10 | 7.6 | 1.3 | 18 | 8 | 3.22 | 0.46 |
| Cass. div. ramp | 0.21 | 0.01 | 27.5 | 1.3 | 3.07 | 0.02 | 3.28 | 0.48 | 20.2 | 0.9 | 11 | 4 | 1.85 | 0.17 |

Notes: Mean (M) best-fitting particle size distribution parameters and their standard deviations (SD) are determined over the entire ring region. Optical depths are from the UVIS occultation of $\alpha\text{Arae}321$.

many-particle-thick (single-scattering) ring model is a better fit to the measured optical depths. The many-particle-thick ring model, where τ_N is given by Eq. (9), is recovered from the thin-layers model in the limit of large N .

In the model, N represents the number of adjacent layers between which multiple particle scattering can occur. N should be thought of as the average number of scattering events which contribute significantly to the forward-scattered signal and not the number of layers of the largest ring particles though a loose comparison between N and the number of particle layers could be drawn for the particles of radius $a \sim \lambda_{\text{avg}}$ (~ 3.4 cm). Our best-fitting N is consistent with a single monolayer of the largest ring particles throughout the C ring and Cassini Division.

Throughout the background C ring and the C ring ramp we find mean values of $a_{\text{min}} \sim 4.15$ mm (Fig. 6a), consistent with Harbison et al. (2013) who used VIMS solar occultations together with $q \sim 3.1$ from Zebker et al. (1985) and $a_{\text{max}} = 10$ m to constrain a_{min} over the background C ring.

Folding in a_{eff} from Colwell et al. (2018), we find $a_{\text{max}} \sim 11.0$ m (Fig. 6a), larger than values reported by Marouf et al. (1983) and Zebker et al. (1985) who found $a_{\text{max}} \sim 4.5$ m in the central C ring using the

direct inversion of the Voyager S-band radio signal, and also slightly larger than French and Nicholson (2000) who reported $a_{\text{max}} \sim 10$ m. We find a slightly steeper power law index than previous studies by Marouf et al. (1983), Zebker et al. (1985), Showalter and Nicholson (1990), and French and Nicholson (2000) who consistently reported $q \sim 3.1$. The mean best-fit power-law index across the background C ring is of $q \sim 3.16$ (Fig. 6c). These studies did not have the resolution to report size distribution parameters in the C ring plateaus, which have widths of ~ 100 km. We find a shallower power law index systematically across the C ring plateaus with a mean value $q \sim 3.05$, (Fig. 7c) which partly explains their larger optical depths compared to the background C ring.

n_0 , which in this study represents the number of $a_0 = 10$ cm particles in a one square meter column of the rings and perpendicular to the ring plane, normalizes the power-law size distribution and is therefore directly proportional to the normal optical depth. We find best-fit $n_0 \sim 36 \times \tau_{\text{UVIS}}$ across the C ring, including the plateaus, except in the outer C ring ramp where n_0/τ_{UVIS} gradually decreases from 36 at a ring radius of 91,000 km to ~ 25 immediately interior to the B ring inner edge (Fig. 6d).

Optical depths in the inner plateaus (P1–P4) generally fit $N \sim 6$

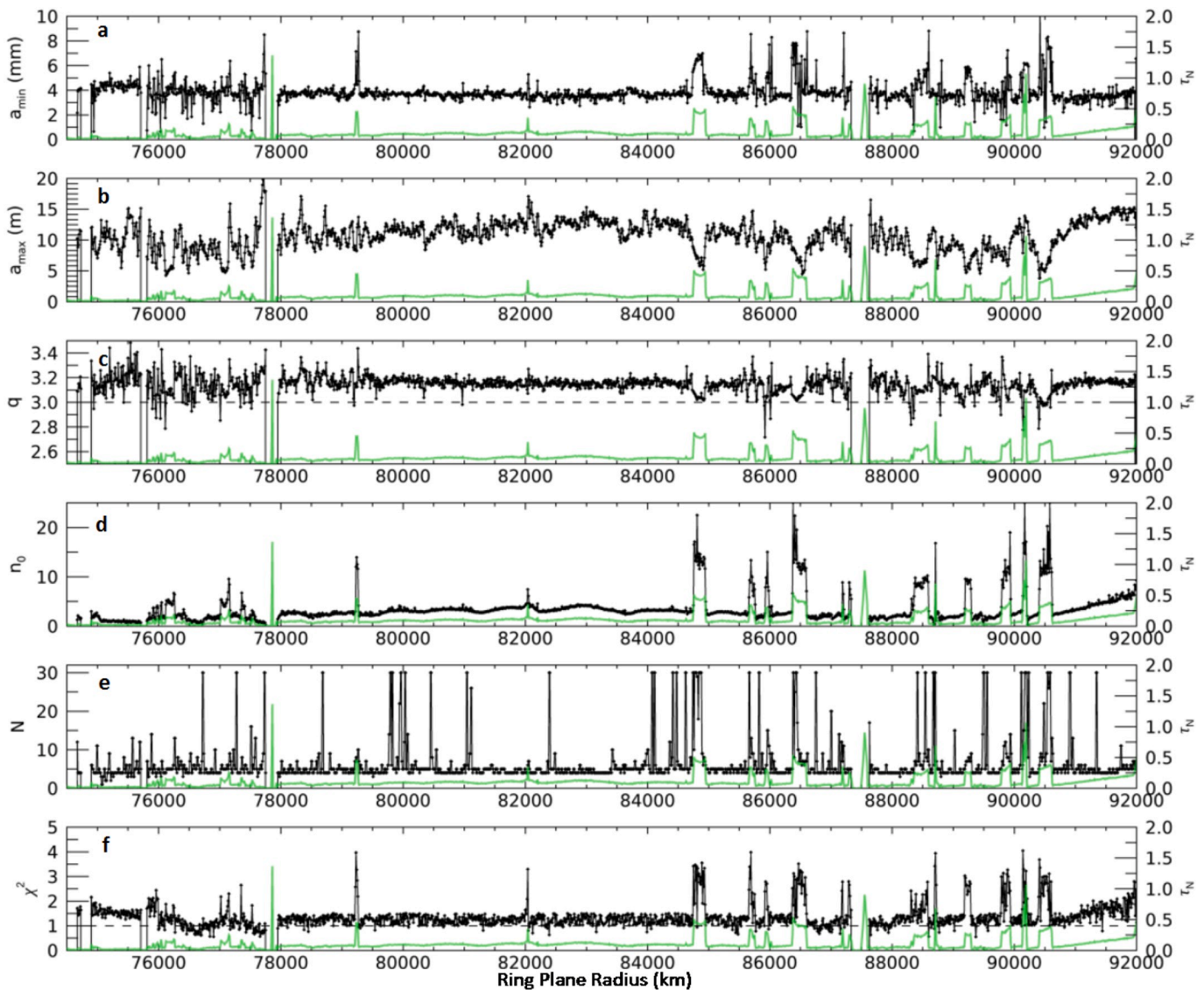


Fig. 6. Best fit parameters for the thin-layers ring model throughout the C ring at 10 km resolution. A_{max} was determined from a_{min} , q , and a_{eff} . Normal optical depth from the UVIS occultation of α Arac32I are also shown in green for reference. Dashed lines show where $q = 3.0$ (c) and where $\chi^2 = 1$ (f). (For interpretation of the references to colour in this figure legend, the reader is referred to the web version of this article.)

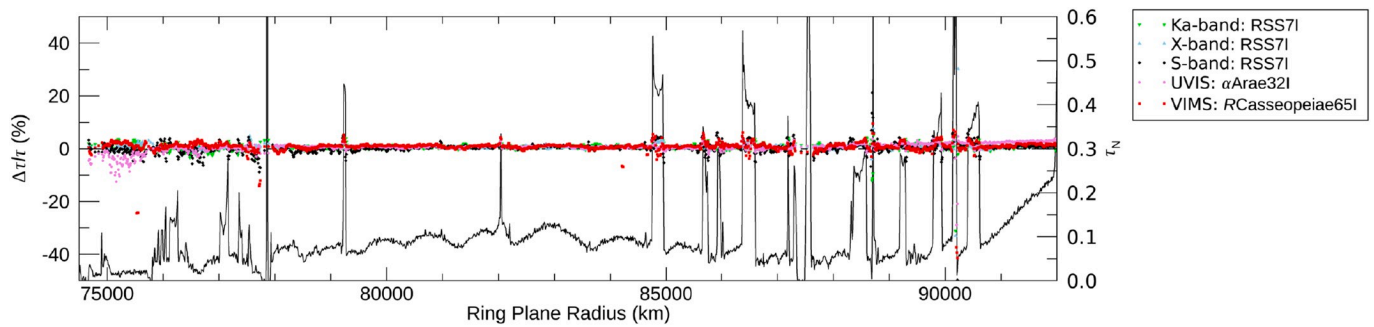


Fig. 7. Fractional difference between model-computed and measured normal optical depth from five profiles of the C ring. Points are separated by 10 km in ring radius. Fractional differences were generally $<10\%$ for occultations at any wavelength. τ_N from the UVIS occultation of α Arae321 is also plotted for reference to the morphological features of the C ring.

layers, similar to the background C ring. The outer plateaus (P5–P11) except for P9 fit $N > 8$ at the center and $N > 30$ layers at their edges where the optical depths are the largest at all wavelengths. In plateaus P1 – P3 as well as P7 and P8 (excluding regions immediately surrounding strong density waves) we find $a_{\min} \sim 4.25$ mm, similar to the background C ring. The rest of the plateaus have larger $a_{\min} \sim 6$ mm while the largest particles in the plateaus are $a_{\max} \sim 6.5$ m, smaller than those in the background C ring by a factor of two. We find the trend $n_0/\tau_{\text{UVIS}} \sim 36$ in the background C ring continues throughout the C ring plateaus.

The C ring ramp has similar best-fit size parameters to the background C ring with $q \sim 3.16$ and $a_{\min} \sim 4.1$ mm. a_{\max} rises with optical depth through the C ring ramp from ~ 9 m outward of P11 to ~ 15 m inward of the B ring inner edge though the other size distribution parameters do not show the same trend. Zebker et al. (1985) determined that the largest particles in the C ring ramp were ~ 4.0 m in radius. Our results on the upper cutoff in particle radius are similar to French and Nicholson (2000) who reported $a_{\max} \sim 10$ m over the C ring ramp. We constrain a_{\max} with the excess variance of UVIS occultations (Colwell et al., 2018) which is also sensitive to particle aggregates that are larger than the largest individual ring particles. One explanation of the trend of increasing a_{\max} with ring radius in the C ring is an increased abundance of particle aggregates approaching the B ring inner edge although UVIS occultations do not show the characteristic variation of apparent normal optical depth with B that is indicative of self-gravity wakes in this region.

The model does not fit the measured optical depths as well inward of $\sim 76,000$ km where optical depths are quite low or in the outer C ring ramp exterior to $\sim 91,000$ km, where χ^2 is a factor of 2–3 larger than those in the background C ring. Plateaus P4–P11 except for P8 also have $\chi^2 \sim 3$ larger than the central background C ring. Generally, model computed and measured optical depths agree with $<10\%$ difference. Fractional differences between model-computed and measured normal optical depths are shown for 5 profiles of the C ring in Fig. 7. Larger fractional differences in optical depth are likely due to the enhanced effect of systematic errors in the determination of I_0 (VIMS and UVIS occultations), and the free-space power (RSS occultations) where $\tau_{\text{UVIS}} < 0.05$. Fractional differences in τ for the UVIS occultation of α Arae321 are also larger and positive in the C ring ramp. Positive $\Delta\tau/\tau$ indicates that model computed optical depth is below measured optical depth. An overestimate of τ_{UVIS} could be due to systematic errors in the optical depth calibration, the nonuniform distribution of particles across the UVIS FOV which would affect Q_{ext} , or the presence of sub-micron particles in this region.

The model finds distinct local minima in χ^2 . Several contours χ^2 at morphologically dissimilar regions of the C ring are shown in Fig. 8. We estimate our errors in each of the parameters as the surface at which χ^2 is larger than its best-fit value by a factor of two. This method suggests that our uncertainty in a_{\min} is $\sim \pm 1$ mm in regions where the minimum value

of $\chi^2 \sim 1$ and $\sim \pm 2$ –3 mm in regions where the minimum value of $\chi^2 \sim 3$. In the plateaus, our uncertainty in q is ~ 0.05 while in the background and C ring ramp our uncertainty in q is as large as 0.15. The standard deviations in parameters measured at 10-km intervals over each ring region are comparable to these errors estimated from the χ^2 contours.

Regions where $\chi^2 \gg 1$ suggest that either the model is not an optimal fit to the data or that the errors in measured optical depths are underestimated. As with the RSS occultations, systematic errors in VIMS and UVIS optical depths manifest from the difficulty in estimating the unocculted star signal after the removal of background signal at each radial location in the rings. Further, RSS variances were estimated from the variance in optical depths over narrow ring regions and could in principle be underestimates of the errors. Throughout the Cassini Division and in the C ring plateaus, where χ^2 is large, fractional differences between model-computed and measured normal optical depths remain below $\sim 10\%$, similar to regions where $\chi^2 \sim 1$.

4.2. The Cassini division

The Cassini Division, while sharing many similar features with the C ring, is distinct in its particle size distribution. Here, q is systematically smaller, and the size distribution is truncated at a smaller a_{\max} except for in the Cassini Division ramp where a_{\max} is significantly larger than anywhere in the C ring. We find $q \sim 3.0$ (Fig. 9c) fits the low optical depth regions and $q \sim 2.94$ in the triple band. In the roughly 150 km immediately exterior to the triple band feature, we find $q \sim 3.15$. This is the only region in the Cassini Division where the power-law index is as steep as the background C ring. Throughout the rest of the Cassini Division ramp q increases with τ , following the same trend as a_{\max} .

In the background Cassini Division, $a_{\min} \sim 4.2$ mm (Fig. 9a) and $a_{\max} \sim 8.9$ m (Fig. 9b). In the ramp, the best-fit a_{\max} is larger by a factor of two which, like the outer C ring ramp, could be due to an increase in the abundance of particle aggregates approaching the inner edge of the A ring. In the Cassini Division ramp, $a_{\min} \sim 3.8$ mm. We find a similar scaling for the number of 10 cm particles, $n_0 \sim 38 \times \tau_{\text{UVIS}}$ (Fig. 9d), throughout the background Cassini Division and $N \sim 5$ (Fig. 9e). Colwell et al. (2009a, 2009b) constrained the scale height of the rings to < 6 m using the dispersion of five density waves in the Cassini Division and $N \lesssim 10$ is consistent with a single layer of the largest ring particles.

Similar to the morphologically distinct regions of the C ring, the model finds poorer fits in the triple band feature and outer Cassini Division ramp ($\chi^2 \sim 3$) although the fractional differences between model-computed and measured normal optical depths are still less than $\sim 10\%$ (Fig. 10). Like the C ring plateaus, the best-fitting a_{\min} throughout the triple band feature are larger than in the background Cassini Division however the model does not fit the measured optical depths as well. In the outer half of the triple band feature and in the outer portion of the Cassini Division ramp, discrepancies between UVIS apparent optical depths are larger than elsewhere in the Cassini Division and show an

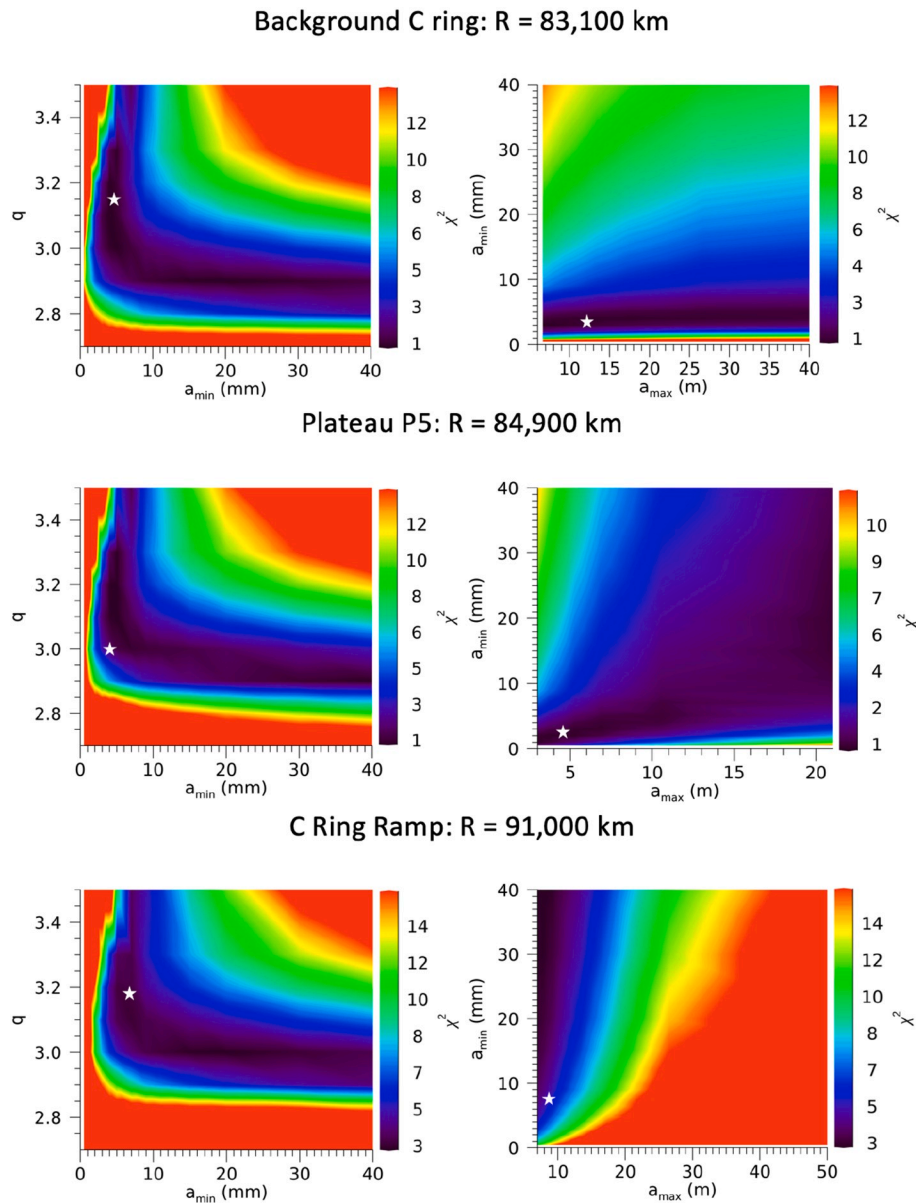


Fig. 8. χ^2 contours at three locations in the C ring. Distinct local minima in χ^2 are found for each of the parameters. In some cases, the figures have been truncated to show only the region immediately surrounding the minimum in χ^2 . Stars show the best-fit parameters, the minima in the cross-sections of χ^2 .

increasing trend with B for occultations at incidence angles below 15° (Fig. 12). Contours of χ^2 for the three morphologically dissimilar regions of the Cassini Division are shown in Fig. 11.

Using surface mass densities from Colwell et al. (2009a, 2009b), we estimate that the Toomre critical wavelengths (most unstable wavelength for gravitational collapse) in the triple band and outer portion of the Cassini Division ramp range from ~ 5 – 7 m, larger than any other regions discussed in this study by at least a factor of two. Particles smaller than the Toomre critical wavelength may aggregate into self-gravity wakes, which impose viewing geometry dependence on UVIS normal optical depths (Colwell et al., 2006, 2007; Jerousek et al., 2016). Such dependence in the outermost hump of the triple band feature is shown in Fig. 12. The trend of increasing τ with ring opening angle, B is not seen in the inner portion of the Cassini Division ramp. Fig. 12 also shows the geometry dependence of normal optical depths in the central A ring (where self-gravity wakes are prevalent) for comparison, though the central A ring is not a focus of this study.

Accurately determining size distribution parameters in regions affected by self-gravity wakes requires detailed modeling of the effects

that self-gravity wakes impose on τ . Jerousek et al. (2016) used the rectangular cross-section self-gravity wake model of Colwell et al. (2007) to constrain the size of the smallest particles in the gaps between opaque self-gravity wakes in the A and B rings. We defer this more detailed analysis of the triple band feature and outer Cassini Division ramp to a future study.

4.3. Beyond a simple power law

Throughout both the background C ring and background Cassini Division, fractional differences between model-computed and measured normal optical depth (Figs. 7, 10) for RSS S-band (13 cm wavelength) systematically negative ($M = -1.5\%$, $SD = 3.3\%$), indicating that the model slightly over predicted S-band optical depths. Since a significant fraction of the ring particles have radii an order of magnitude smaller than the S-band wavelength, $Q_{\text{ext}} \sim 0$, and these small particles contribute little to the S-band optical depth. But at Ka-band (0.94 cm) wavelengths, particles $> \sim 1$ cm contribute significantly to the measured normal optical depth. Therefore, the significantly smaller S-band optical

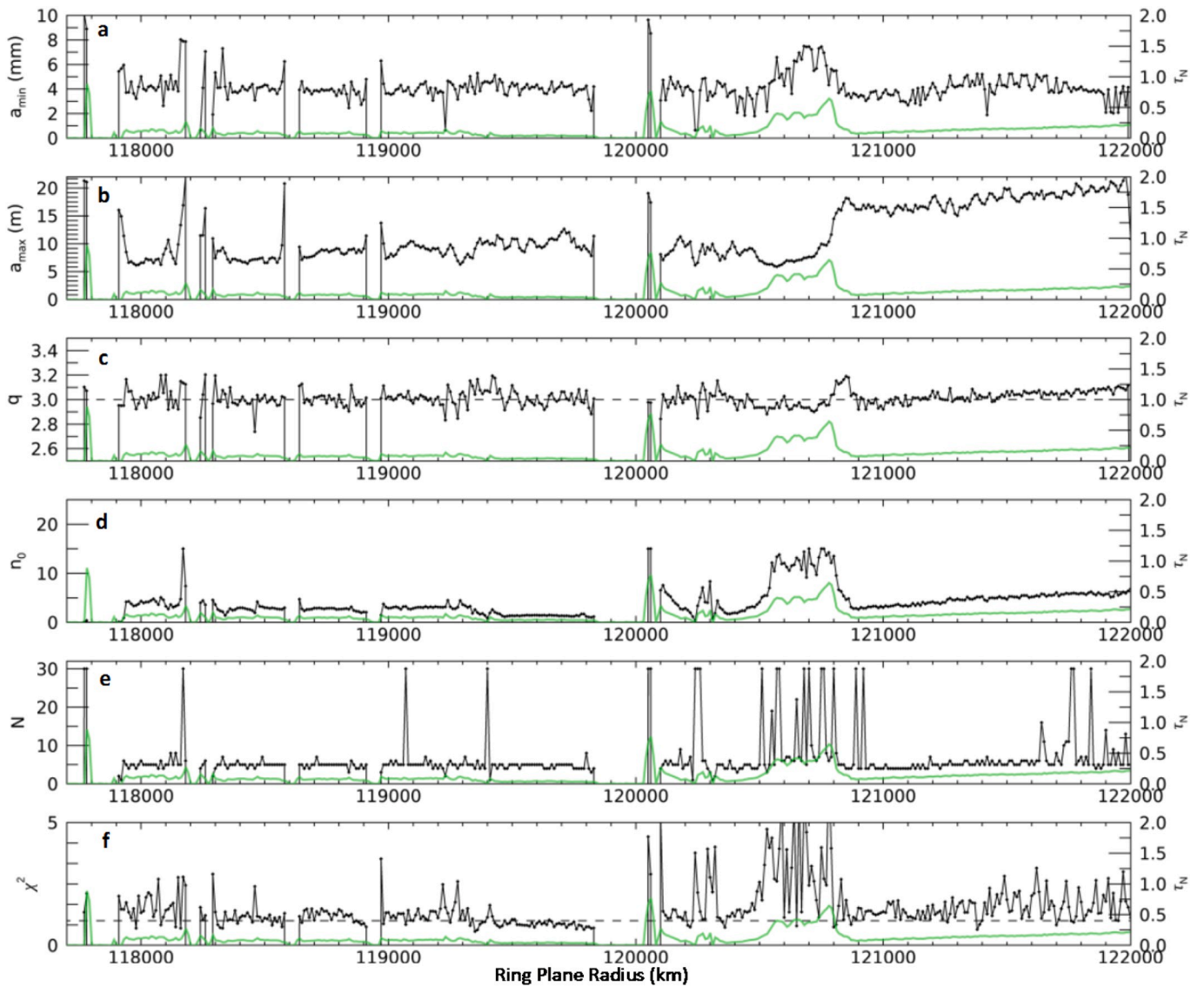


Fig. 9. Best fit parameters for the thin-layers ring model throughout the Cassini Division at 10 km resolution. a_{max} was determined from a_{min} , q , and a_{eff} . Normal optical depth from the UVIS occultation of α Arae32I are also shown in green for reference. (For interpretation of the references to colour in this figure legend, the reader is referred to the web version of this article.)

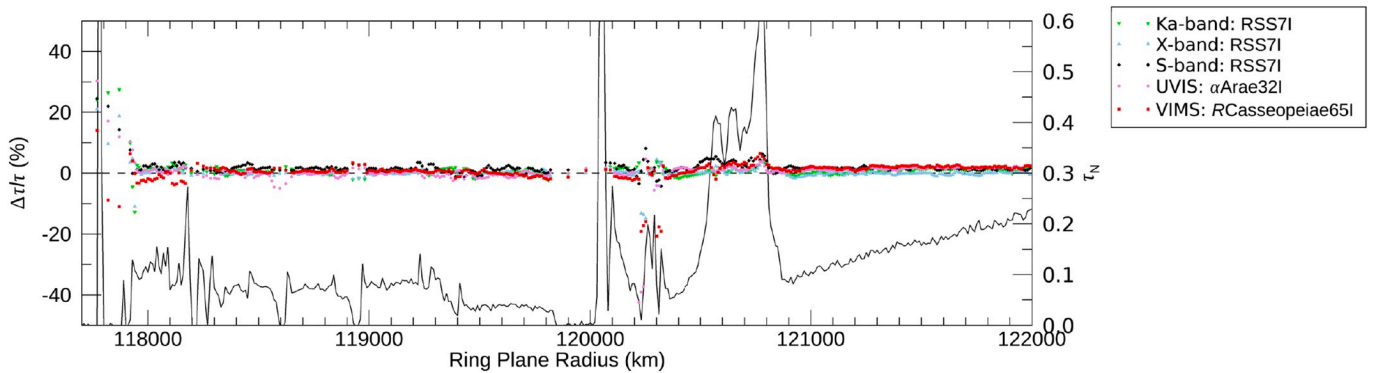


Fig. 10. Fractional difference between model-computed and measured normal optical depth from five profiles of the Cassini Division. Points are separated by 10 km in ring radius. Fractional differences are generally $<10\%$ for occultations at any wavelength. τ_N from the UVIS occultation of α Arae32I is also plotted for reference to the morphological features of the Cassini Division.

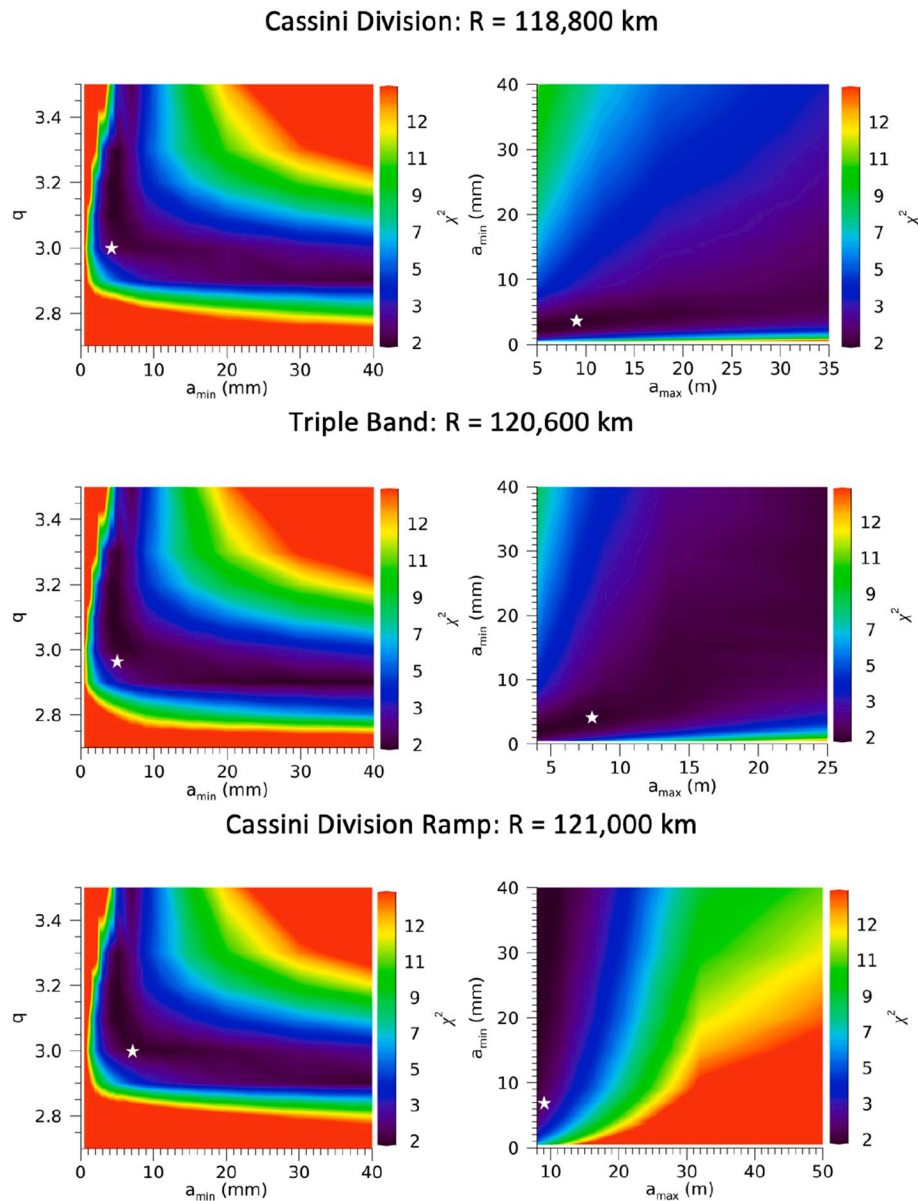


Fig. 11. χ^2 contours at three locations in the Cassini Division. Distinct local minima in χ^2 are found for each of the parameters. In some cases, the figures have been truncated to show only the region immediately surrounding the minimum in χ^2 . Stars indicate the best-fit parameters, the minima in the cross-sections of χ^2 .

depths that we detect compared to Ka-band optical depths indicate the presence of such smaller particles. We were therefore motivated to check whether adding two additional free parameters, a_{bend} , and q_2 would improve the goodness of fit. In a piecewise-continuous size distribution, the power-law index is steepened for $a \geq a_{\text{bend}}$, with $q_2 > q$. The number of particles in radius interval $[a, a + da]$ in this new distribution is given by:

$$n(a) = \begin{cases} C_1 a^{-q}, & a_{\text{min}} \leq a \leq a_{\text{bend}} \\ C_2 a^{-q_2}, & a_{\text{bend}} < a \leq a_{\text{max}} \end{cases}, \quad (22)$$

where $C_2 = C_1(a_{\text{bend}})^{q_2 - q}$. Brooks et al. (2004) introduced this piecewise-continuous power-law to fit Galileo NIMS data of Jupiter's main ring, since successively larger particles in the micron size range contributed far less to measured optical depths than would be predicted by a simple power-law. However, fitting the UVIS, VIMS, and RSS optical depth profiles of Saturn's C ring and Cassini Division with this two-component power-law size distribution did not significantly reduce χ^2 at most locations in the C ring or Cassini Division. For the C ring plateaus, the best-fit $a_{\text{bend}} \sim a_{\text{max}}$; in other words, the two-component model essentially returned a single

component power-law size distribution consistent with our initial simple model.

5. Discussion

While the plateaus exhibit significant optical depth differences from the background C ring, these differences are partially explained by the variation in size distribution parameters and partially by the larger particle number density. In the C ring plateaus, where optical depths are larger than the C ring background by a factor of several, the power law index is shallower and the upper cutoff on particle size, a_{max} , is smaller than in the background C ring. Both factors cause the cross-section weighted particle size, a_{eff} , to be smaller in the plateaus. This collection of smaller particles with similar surface mass presents a larger cross-sectional area and therefore a significantly larger optical depth. The same explanation applies to the comparison of the triple band feature of the Cassini Division with the Cassini Division's lower optical depth regions. In the triple band feature, again we find a shallower power-law index as well as smaller a_{max} .

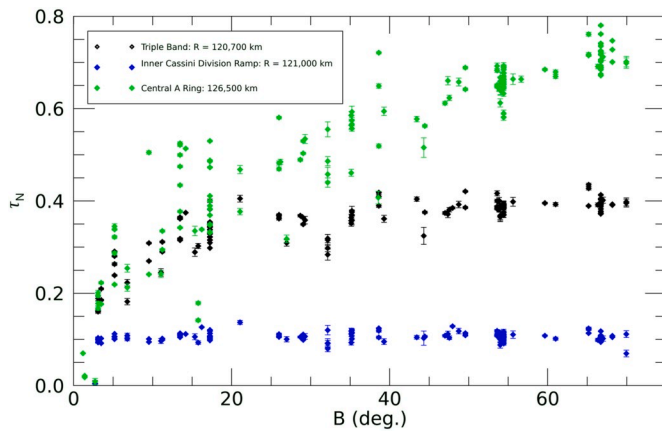


Fig. 12. τ_N vs. B for UVIS occultations in three ring regions: the triple band (black), the inner Cassini Division ramp (blue), and the central A ring (green), where self-gravity wakes have the most pronounced effect on normal optical depths.

The average power-law index in the background Cassini Division is systematically lower than in the background C ring by ~ 0.1 , with smaller particles contributing more to the normal optical depth. The best-fit minimum particle size is also slightly smaller $\sim 2\text{--}3$ mm than in the C ring. The best-fit maximum particle size is smaller in the lower optical depth regions of the Cassini Division but larger in the Cassini Division ramp although the presence of self-gravity wakes could contribute systematic errors to the fitting of size distribution parameters in this region.

5.1. Particle sorting between the C ring plateaus and background

In each of the C ring plateaus, the upper cutoff of the size distribution, a_{\max} , is less than half of the mean value in the background C ring. This combined with the shallower $q \sim 3.05$ in the plateaus explains the dramatic difference in normal optical depth between the two regions. Smaller particles have a larger cross-sectional area per unit mass and block a larger fraction of the incident flux, as long as they are significantly larger than the measured wavelength. Dramatic differences in several of the size distribution parameters between the background C ring and plateaus suggests some mechanism is relegating the larger particles to the lower optical depth regions of the C ring (Hedman and Nicholson, 2013; Tiscareno et al., 2013a). Further clues are provided by azimuthally limited gaps known as “ghosts” in the C ring plateaus in high resolution UVIS stellar occultations (Baillié et al., 2013) and by streaky texture seen in particle tracking images from the ring grazing orbits of Cassini (Tiscareno et al., 2019).

Baillié et al. (2013) identified 35 regions <5 samples wide where the HSP photon count rate was within 35% of the unocculted star signal in the C ring plateaus. They dubbed these holes in the intervening ring material “ghosts” and proposed that they are azimuthally limited gaps opened by ring particles or particle aggregates that are less than ~ 50 m across. They suggested that these gaps are opened by the same process that opens azimuthally limited gaps around propeller objects in the A ring (Tiscareno et al., 2008). Baillié et al. (2013) used strict criteria for identifying ghosts in the C ring. It is possible that many smaller ghosts are present in the C ring plateaus that are not fully resolved in the UVIS HSP occultation data. Additionally, Baillié et al. (2013) excluded regions in the plateaus P5, P6, P7, and P10 from their search because spiral density waves that had previously been identified by Baillié et al. (2011) and Colwell et al. (2009a, 2009b) complicate the criteria for detection. Fig. 13 shows the UVIS normal optical depth of plateau P4 measured by the α Virginis34I occultation at $B = 17^\circ$ above the ring plane at 31 m radial resolution. Several of the ghosts reported by Baillié et al. (2013) are shown in detail in the window. However, hundreds of points where

the normal optical depth is greater than 5σ below the mean value of $\tau_N \sim 0.42$ can also be seen in this region. These could be unresolved ghosts either because their intrinsic widths are <43 m, or because the occultation cut across a narrower or partially filled region of the propeller lobe. But they could also be regions of temporarily lower than average surface mass density due to statistical fluctuations in the particle arrangement at the scale of the UVIS HSP integration area.

Estimates by Sremčević et al. (2002) and Tiscareno et al. (2008) stated that the radial extent of the primary propeller lobe grows linearly with the boulder radius according to:

$$\Delta r \approx 3r_H, \quad (23)$$

where r_H is the boulder’s Hill radius, $r_H = a_{\text{boulder}}(M_{\text{boulder}}/3M_{\text{Saturn}})^{1/3}$. This suggests that the particles that produce the ghosts are <15 m in radius, comparable to the sizes of the largest particles in the background C ring. However, for the propeller-like gap to open, the boulder or moonlet must be ~ 3 times larger than the largest particles in a continuous power-law size distribution (Lewis and Stewart, 2009). It appears that propeller features in the C ring plateaus are opened by boulders or aggregates that are as large as boulders or aggregates in the neighboring C ring background. One explanation for the difference in particle sizes is increased aggregation in the lower optical depth regions. If 10–20 m particle aggregates are ubiquitous in the background C ring, they will contribute significantly to the measured normal optical depth but their mass and proximity to one another will disturb the formation of propeller lobes in their vicinity. However, in the plateaus, where these 10–20 m particle aggregates are sparse, they will contribute little to the measured optical depth and their large mass compared to their local ring region of smaller particles will allow them to open propeller lobes.

In the Cassini Division’s triple band, the largest particles ($a_{\max} \sim 7$ m) are similar in size to those in the neighboring background Cassini Division, interior to the feature. Exterior to the triple band feature and throughout the Cassini Division ramp, the largest particles are ~ 14 m in radius. Baillié et al. (2013) also found 265 ghosts in the triple band feature and Cassini Division ramp with radial widths ranging from 1.7–375 m. Ghost width is proportional to the boulder’s mass, with larger boulder sizes in the Cassini Division likely due to decreased tidal forces at greater distances from Saturn.

5.2. Surface density from spiral density wave dispersion

Ring opacity measurements from the dispersion of spiral density waves also provide a constraint on the size distribution parameters. Ring opacity is given by

$$\kappa = \frac{\tau_g}{\sigma}, \quad (24)$$

where τ_g is the geometric optical depth and σ is the local surface mass density of the rings. The inverse of opacity, κ^{-1} , can be determined analytically for the power law size distribution and is given by

$$\frac{1}{\kappa} = \frac{\int_{a_{\min}}^{a_{\max}} \rho \frac{4}{3} \pi a^3 n(a) da}{\int_{a_{\min}}^{a_{\max}} \pi a^2 n(a) da} = \frac{4(3-q)}{3(4-q)} \left[\frac{a_{\max}^{4-q} - a_{\min}^{4-q}}{a_{\max}^{3-q} - a_{\min}^{3-q}} \right] \rho. \quad (25)$$

This allows us to combine our measurements of the particle size distribution with surface mass density measurements from the dispersion of spiral density waves to estimate the bulk particle density, ρ . Hedman and Nicholson (2013) determined σ in 13 spiral density waves driven by outer Lindblad resonances with Saturn’s normal modes in the C ring. Four of these resonances are in plateaus. Baillié et al. (2011) also determined σ in 5 spiral density waves driven by inner Lindblad resonances with moons exterior to Saturn’s rings and studied two waves in plateaus. Although the optical depths of the plateaus are larger than the background C ring by a factor of several, the surface mass density estimates of both studies indicate similar values in both regions. Hedman and Nicholson (2013) indicate that the largest surface mass densities are

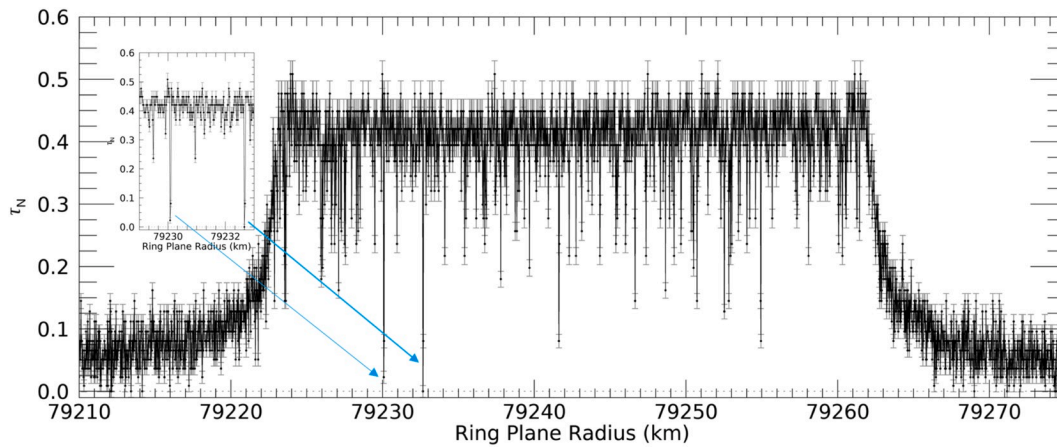


Fig. 13. Optical depths at 31 m resolution across the plateau, P4 from α Virginis341 occultation (UVIS). $1\text{-}\sigma$ error bars are shown in grey.

in the central background C ring where $\tau \sim 0.15$. Inverse opacities from the power-law parameters assuming a nominal $\rho = 1 \text{ g/cm}^3$ particle density are also shown in Table 2.

We fit surface densities determined at these 18 locations spanning the C ring from Hedman and Nicholson (2013) and Baillié et al. (2011) and 5 locations in the Cassini Division from Colwell et al. (2009a, 2009b) to the volume integrated particle area from our best-fit particle size distribution parameters in order to constrain ρ , the average ring particle density. Surface mass densities from Hedman and Nicholson (2013), Baillié et al. (2011) and from the best-fit values of ρ and our size distribution parameters are shown across the C ring in Fig. 14 and across the Cassini Division in Fig. 15. We find that in the inner and outer C ring, particles appear to be highly porous, with densities less than a few tenths that of crystalline water ice. Table 1 shows ρ at each of the radial locations where surface mass density estimates were available. This would require the particles to have significant material strength in order to

hold themselves together. Another likely explanation for the extremely small densities is that the largest particles in our size distribution are not individual ring particles but particle aggregates or ephemeral clusters of particles. Porco et al. (2004) give the Roche critical density as

$$\rho_{\text{crit}} = \frac{3M_p}{\gamma r^3}, \quad (26)$$

where M_p is the mass of Saturn, r is the semi-major axis and γ is a dimensionless parameter so that the volume of the particle is γa^3 . For a particle that fills its Roche lobe, $\gamma \sim 1.6$. At a given distance from Saturn, a ring particle with a density less than ρ_{crit} will be pulled apart by tidal forces unless it has sufficient internal material strength to hold itself together. In ring regions where there is ample material available for accretion and collisions are relatively gentle, a ring particle with $\rho > \rho_{\text{crit}}$ will accrete a porous mantle until its density decreases to ρ_{crit} (Tiscareno

Table 2

Simple power-law parameters at the locations of density waves for which σ can be measured.

| Study | Radius (km) | σ (g/cm ²) | κ (cm ² /g) | τ_N | n_0/τ_{UVIS} | | a_{min} (mm) | | a_{max} (m) | | q | | ρ (g/cm ³) | ρ_{crit} (g/cm ³) |
|------------------------|-------------|-------------------------------|-------------------------------|----------|--------------------------|------|-----------------------|------|----------------------|------|------|------|-----------------------------|---|
| | | | | | M | SD | M | SD | M | SD | M | SD | | |
| C ring density waves | | | | | | | | | | | | | | |
| B2011 | 74,892 | 5.8 | 0.06 | 0.03 | 40 | 0.5 | 4.8 | 1.1 | 10.8 | 1.3 | 3.15 | 0.05 | 0.28 | 2.54 |
| B2011 | 77,511 | 6.0 | 0.11 | 0.07 | 31 | 0.4 | 3.4 | 0.6 | 7.3 | 1.2 | 3.09 | 0.03 | 0.25 | 2.29 |
| HN2014 | 80,998 | 58.5 | 0.02 | 0.10 | 37 | 0.2 | 4.2 | 0.4 | 10.8 | 1.0 | 3.13 | 0.03 | 1.01 | 2.01 |
| HN2014 | 82,010 | 56.8 | 0.03 | 0.16 | 33 | 1.2 | 5.7 | 2.8 | 12.6 | 1.3 | 3.14 | 0.02 | 0.94 | 1.93 |
| HN2014 | 82,061 | 101.6 | 0.02 | 0.17 | 34 | 1.4 | 5.9 | 3.6 | 14.8 | 1.8 | 3.16 | 0.03 | 1.16 | 1.93 |
| HN2014 | 82,209 | 69.2 | 0.01 | 0.10 | 36 | 0.3 | 4.1 | 0.6 | 11.7 | 1.5 | 3.14 | 0.03 | 1.05 | 1.92 |
| HN2014 | 83,633 | 49.5 | 0.02 | 0.08 | 35 | 0.2 | 3.5 | 0.3 | 11.1 | 1.6 | 3.13 | 0.04 | 0.93 | 1.82 |
| HN2014 | 84,644 | 40.5 | 0.02 | 0.09 | 34 | 0.3 | 4.0 | 0.6 | 11.5 | 1.4 | 3.12 | 0.04 | 0.74 | 1.76 |
| HN2014 | 84,814 | 39.4 | 0.11 | 0.44 | 36 | 2.7 | 6.3 | 3.4 | 5.7 | 0.7 | 3.04 | 0.01 | 0.37 | 1.75 |
| HN2014 | 84,857 | 22.4 | 0.19 | 0.43 | 38 | 1.7 | 6.4 | 3.9 | 5.6 | 0.7 | 3.04 | 0.01 | 0.31 | 1.74 |
| HN2014 | 86,400 | 47.0 | 0.09 | 0.43 | 34 | 3.3 | 7.0 | 2.1 | 7.2 | 0.2 | 3.00 | 0.06 | 2.00 | 1.65 |
| HN2014 | 86,576 | 11.8 | 0.27 | 0.32 | 40 | 5.1 | 6.9 | 2.9 | 10.3 | 6.6 | 3.19 | 0.11 | 0.13 | 1.64 |
| HN2014 | 87,189 | 14.1 | 0.09 | 0.13 | 32 | 1.8 | 4.5 | 1.2 | 10.7 | 2.4 | 3.10 | 0.13 | 0.15 | 1.61 |
| B2011 | 87,647 | 2.2 | 0.20 | 0.04 | 45 | 1.7 | 5.3 | 1.1 | 10.8 | 1.8 | 3.25 | 0.07 | 0.19 | 1.58 |
| B2011 | 89,883 | 13.1 | 0.28 | 0.36 | 35 | 1.1 | 4.9 | 1.0 | 6.3 | 2.6 | 3.08 | 0.07 | 0.20 | 1.47 |
| B2011 | 89,894 | 14.2 | 0.26 | 0.36 | 35 | 1.1 | 4.9 | 1.0 | 6.3 | 2.6 | 3.08 | 0.07 | 0.22 | 1.47 |
| Cassini division waves | | | | | | | | | | | | | | |
| C2009 | 118,075 | 11.0 | 0.11 | 0.12 | 36 | 0.6 | 5.3 | 0.6 | 7.2 | 1.1 | 3.05 | 0.05 | 0.60 | 0.65 |
| C2009 | 118,460 | 9.8 | 0.08 | 0.08 | 37 | 0.4 | 5.4 | 1.0 | 7.1 | 0.3 | 2.97 | 0.04 | 0.45 | 0.64 |
| C2009 | 118,840 | 13.1 | 0.06 | 0.07 | 38 | 0.3 | 5.0 | 0.5 | 8.6 | 0.4 | 3.00 | 0.03 | 0.31 | 0.63 |
| C2009 | 120,060 | 57.6 | 0.04 | 0.26 | 19 | 4.0 | 5.9 | 4.0 | 7.7 | 1.6 | 2.94 | 0.08 | 0.68 | 0.62 |
| C2009 | 120,680 | 35.1 | 0.11 | 0.39 | 34 | 1.5 | 5.9 | 1.1 | 8.0 | 1.1 | 2.94 | 0.03 | 0.17 | 0.61 |
| T2007 | 121,250 | 11.0 | 0.13 | 0.14 | 33 | 0.4 | 4.9 | 2.6 | 17.0 | 1.1 | 3.02 | 0.01 | 0.05 | 0.60 |

Notes: Mean (M) best-fitting particle size distribution parameters and their standard deviation (SD) are determined over 8-point (80 km) intervals centered on the radial location of each wave. Average particle densities are determined by dividing surface mass densities derived from spiral density wave dispersion by the volume-integrated particle density using the best-fit particle size distribution parameters. Opacities, κ are reported from studies of density wave dispersion by Colwell et al. (2009a, 2009b) (C2009), Baillié et al. (2011) (B2011), Hedman and Nicholson (2014) (HN14), Tiscareno et al. (2013a, 2013b) (T2013). Optical depths are from the UVIS occultation α Arae321.

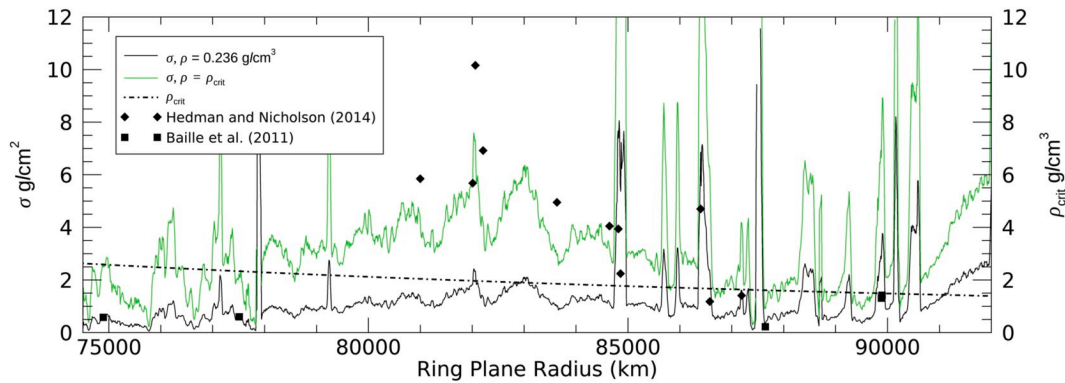


Fig. 14. C ring surface mass densities computed by integrating particle masses over the size distribution assuming nominal bulk particle densities of 0.236 g/cm^3 (black) and using the Roche critical density, ρ_{crit} (green). ρ_{crit} is also shown at each location (dashed line). Surface mass densities from spiral density wave dispersion (Baillié et al., 2011; Hedman and Nicholson, 2014) are shown as black squares and diamonds respectively. (For interpretation of the references to colour in this figure legend, the reader is referred to the web version of this article.)

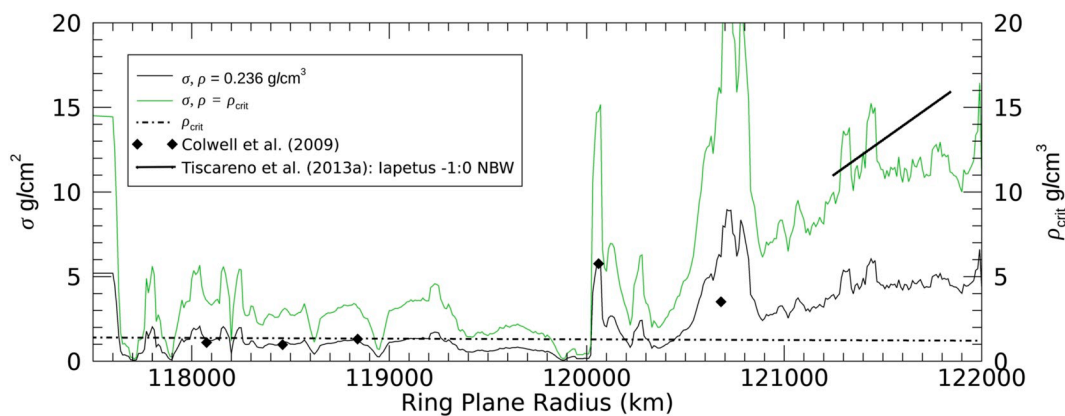


Fig. 15. Cassini Division surface mass densities computed by integrating particle masses over the size distribution assuming nominal bulk particle densities of 0.23 g/cm^3 (black) and using the Roche critical density, ρ_{crit} (green). ρ_{crit} is also shown at each location (dashed line). Surface mass densities from spiral density wave dispersion (Colwell et al., 2009a, 2009b) are shown as black diamonds. Surface mass densities from the dispersion of the lapetus $-1:0$ nodal bending wave (Tiscareno et al., 2013a) are shown as a black line. (For interpretation of the references to colour in this figure legend, the reader is referred to the web version of this article.)

et al., 2013b).

Zhang et al. (2016) used Cassini microwave radiometry to probe the fraction of non-icy material in Saturn's rings. By fitting brightness temperature measurements of Saturn's ring ansa to several ring models they determined that in the inner and outer C ring, particles are 1–2% silicates with porosities of $\sim 75\%$ ($\rho \sim 0.24 \text{ g/cm}^3$). In the central C ring at $\sim 83,000 \text{ km}$ from Saturn's center, they found that the fraction of non-icy material reaches its maximum of $\sim 6.3\%$ using a ring particle composition of intimately mixed ice and silicate. They also considered a silicate core, porous water-ice mantle model. In order to fit opacity estimates using surface densities from Hedman and Nicholson (2014) and Baillié et al. (2011), to their core-mantle particle model, Zhang et al. (2016) suggested that a_{max} should be a factor of 4 or 5 larger than mean values reported by Zebker et al. (1985). Our best-fitting a_{max} and apparent bulk densities derived using our best-fitting size distribution parameters in the central C ring are more consistent with ring opacities from the silicate core-porous icy mantle model than the intimately mixed model.

In the C ring plateaus and the Cassini Division triple band feature the upper cutoff of the size distribution, a_{max} , is smaller than in the low optical depth regions of the C ring and Cassini Division by a factor of at least two. However, in both of these regions, UVIS occultations show the presence of ghosts (Baillié et al., 2013) and “streaky” texture is seen in ISS images on both the lit and unlit sides of the rings (Tiscareno et al., 2019). A likely explanation of both the ghosts and “streaky” texture is a

moderate population of propeller features formed by 5–10 m particles or particle aggregates in these ring regions. This population of 5–10 m particles is large enough to produce the observations of significant numbers of ghosts in UVIS occultation data and streaky texture in ISS images but too small to contribute significantly to the optical depth or surface mass density of these ring regions. In short, these large particles or particle aggregates only sparsely populate the high optical depth regions of the C ring and Cassini Division. This suggests that in the low optical depth regions of the C ring and Cassini Division, well within the Roche zone and in regions where the Toomre critical wavelength (most unstable wavelength for gravitational collapse) is smaller than $\sim 4 \text{ m}$, particle aggregates with diameters of 20–40 m are forming and are ubiquitous enough to contribute substantially to the measured normal optical depth. If this were not the case (that is, if these are not aggregates), large particles must have been selectively removed from the high optical depth regions of the C ring and Cassini Division, which seems unlikely. Larger particle densities due to an increased fraction of rock in the Central C ring might also contribute to particle aggregation well within Saturn's Roche zone.

Overall, we find that the simple power-law size distribution fits the many optical depth profiles measured by Cassini VIMS, UVIS, and RSS throughout Saturn's C ring and Cassini Division well with $N \sim 3\text{--}5$ and larger in the C ring plateaus. Best-fit “bent” power law parameters suggest a moderately steep cutoff in particle radius at $a_{\text{bend}} \sim 1\text{--}2 \text{ m}$ throughout the C ring and Cassini Division, but our relative insensitivity

to the larger sized particles does not allow us to conclude that this six-parameter size distribution is able to fit the measured optical depths better than a simple, four-parameter size distribution.

Combining optical depth profiles measured by multiple instruments on Cassini has proved to be a reliable way to ascertain the regional variation in the particle size distribution in Saturn's rings. In the future, we hope to use the viewing geometry dependence of RSS, VIMS and UVIS optical depth profiles to better constrain the mesoscale particle aggregates in the C ring and Cassini Division including more detailed modeling of the effects of "ghosts" in the C ring plateaus and self-gravity wakes in the triple band feature and outer Cassini Division ramp.

Acknowledgments

This material is based upon work supported by the United States National Aeronautics and Space Administration under Grant No. NNX15AH22G issued through the Cassini Data Analysis Program, and by the Cassini project and the UVIS team. We are indebted to the Cassini Rings Target Working Team and Rings Working Groups whose support for, and integration of, these observations has made this research possible. We are also thankful to Mathew S. Tiscareno and an anonymous reviewer whose suggestions greatly improved the quality of this work.

References

- Baillié, K., Colwell, J.E., Lissauer, J.J., Esposito, L.W., Sremčević, M., 2011. Waves in Cassini UVIS stellar occultations 2. The C ring. *Icarus* 216, 292–308. <https://doi.org/10.1016/j.icarus.2011.05.019>.
- Baillié, K., Colwell, J.E., Esposito, L.W., Lewis, M.C., 2013. Meter-sized moonlet population in Saturn's C ring and Cassini division. *Astron. J.* 145 (171), 2624–2629. <https://doi.org/10.1088/0004-6256/145/6/171>.
- Becker, T.M., Colwell, J.E., Esposito, L.W., Bratcher, A.D., 2015. Characterizing the particle size distribution of Saturn's A ring with Cassini UVIS occultation data. *Icarus* 279, 20–35. <https://doi.org/10.1016/j.icarus.2015.11.001>.
- Brahic, A., Sicardy, B., 1981. Apparent thickness of Saturn's rings. *Nature* 289, 447–450. <https://doi.org/10.1038/289447a0>.
- Brilliantov, N., Krapivsky, P.L., Bodrova, A., Spahn, F., Hayakawa, H., Stadnichuk, V., Schmidt, J., 2015. Size distribution of particles in Saturn's rings from aggregation and fragmentation. *PNAS* 112 (31), 9536–9541, 2015.
- Brooks, S.M., Esposito, L.W., Showalter, M.R., 2004. The size distribution of Jupiter's main ring from Galileo imaging and spectroscopy. *Icarus* 170 (1), 35–57.
- Brown, R.H., Baines, K.H., Bellucci, G., Bibring, J.-P., Burratti, B.J., Bussoletti, E., Capaccioni, F., Cerroni, P., Clark, R.N., Coradini, A., Cruikshank, D.P., Drossart, P., Formisano, V., Jaumann, R., Langevin, Y., Matson, D.L., McCord, T.B., Miller, E., Nelson, R.M., Nicholson, P.D., Sicardy, B., Sotin, C., 2004. The Cassini visual and infrared mapping spectrometer investigation. *Space Sci. Rev.* 115, 111–168.
- Colwell, J.E., Esposito, L.W., Sremčević, M., 2006. Gravitational wakes in Saturn's A ring measured by stellar occultations from Cassini. *Geophys. Res. Lett.* 33, L07201 <https://doi.org/10.1029/2005GL025163>.
- Colwell, J.E., Esposito, L.W., Sremčević, M., Stewart, G.R., McClintock, W.E., 2007. Self-gravity wakes and radial structure of Saturn's B ring. *Icarus* 190, 127–144. <https://doi.org/10.1016/j.icarus.2007.03.018>.
- Colwell, J.E., Cooney, J., Esposito, L.W., Sremčević, M., 2009a. Density waves in Cassini UVIS stellar occultations. 1. The Cassini division. *Icarus* 200, 574–580. <https://doi.org/10.1016/j.icarus.2008.12.031>.
- Colwell, J.E., Nicholson, P.D., Tiscareno, M.S., Murray, C.D., French, R.G., Marouf, E.A., 2009b. The structure of Saturn's rings. In: *Ch. 14: Saturn From Cassini-Huygens*. Springer, pp. 375–412 (doi:10.1007/978-1-4020-9217-6).
- Colwell, J.E., Esposito, L.W., Pettis, D., Sremčević, M., Jerousek, R.G., Bradley, E.T., 2010. Cassini UVIS stellar occultation observations of Saturn's rings. *Astron. J.* 140, 1569–1578. <https://doi.org/10.1088/0004-6256/140/6/1569>.
- Colwell, J.E., Esposito, L.W., Cooney, J.H., 2018. Particle sizes in Saturn's rings from UVIS stellar occultations. 1. Variations with ring region. *Icarus* 300, 150–166. <https://doi.org/10.1016/j.icarus.2017.08.036>.
- Colwell, J.E., Jerousek, R.G., Becker, T.M., Esposito, L.W., 2019. Cassini Orbiter Saturn UVIS Ring Stellar Occultations 2.0, CO-SR-UVIS-2/4-OCC-V2.0, NASA Planetary Data System.
- Cuzzi, J.N., 1985. Rings of Uranus—not so thick, not so black. *Icarus* 63, 312–316.
- Cuzzi, J.N., 1995. Evolution of planetary ring-moon systems; in *Comparative Planetology*, Kluwer Press; also *Earth, Moon, and Planets* 67, 179–208.
- Cuzzi, J. N., J. J. Lissauer, L. W. Esposito, J. B. Holberg, E. A. Marouf, G. L. Tyler, A. Boischoit (1984) Saturn's rings: Properties and Processes; in *Planetary Rings*, R. Greenberg and A. Brahic, eds. University of Arizona Press, Tucson.
- Cuzzi, J., Clark, R., Filachione, G., French, R., Johnson, R., Marouf, E., Spilker, L., 2009. Ring Particle Composition and Size Distribution. *Ch. 15: Saturn From Cassini-Huygens*. Springer (doi:10.1007/978-1-4020-9217-6).
- Dohnanyi, J.W., 1969. Collisional models of asteroids and their debris. *J. Geophys. Res.* 74, 2531–2554.
- Dones, L., 1998. The rings of the giant planets. In: Schmitt, B., de Bergh, C., Festou, M. (Eds.), *Solar System Ices*. Kluwer, Dordrecht, pp. 711–734.
- Dones, L., Cuzzi, J.N., Showalter, M.R., 1993. Voyager photometry of Saturn's A ring. *Icarus* 105, 184–215.
- Dunn, D.E., Molnar, L.A., Fix, J.D., 2002. More microwave observations of Saturn: modeling the ring with a Monte Carlo radiative transfer code. *Icarus* 160, 132.
- Durisen, Richard H., Cramer, Michael Lynn, Murphy, Brian W., Cuzzi, Jeffrey N., Mullikin, Thomas L., Cederbloom, Steven E., 1989. Ballistic transport in planetary ring systems due to particle erosion mechanisms: I. Theory, numerical methods, and illustrative examples. *Icarus*. ISSN: 0019-1035, Volume 80 (Issue 1), 136–166. [https://doi.org/10.1016/0019-1035\(89\)90164-4](https://doi.org/10.1016/0019-1035(89)90164-4).
- Durisen, R.H., et al., 1992. Ballistic transport in planetary ring systems due to particle erosion mechanisms. II. Theoretical models for Saturn's A- and B-ring inner edges. *Icarus* 100, 364–393.
- Durisen, Richard H., Bode, Paul W., Dyck, Stanley G., Cuzzi, Jeffrey N., Dull, James D., White II, James C., 1996. Ballistic Transport in Planetary Ring Systems Due to Particle Erosion Mechanisms: III. Torques and Mass Loading by Meteoroid Impacts. *Icarus*. ISSN: 0019-1035, Volume 124 (Issue 1), 220–236. <https://doi.org/10.1006/icar.1996.0200>.
- Esposito, L.W., Ocallaghan, M., West, R.A., 1983. The structure of Saturn's rings – implications from the voyager stellar occultation. *Icarus* 56, 439–452.
- Esposito, L.W., Barth, C.A., Colwell, J.E., Lawrence, G.M., McClintock, W.E., Stewart, A.I. F., Keller, H.U., Korth, A., Lauche, H., Festou, M.C., Lane, A.L., Hansen, C.J., Maki, J. N., West, R.A., Jahn, H., Reulke, R., Warlich, K., Shemansky, D.E., Yung, Y.L., 2004. The Cassini ultraviolet imaging spectrograph investigation. *Space Sci. Rev.* 115, 299–361 (2004).
- Esposito, L.–W., Rehnberg, M., Colwell, J.–E., Sremčević, M. 2017. Size of Self-Gravity Wakes from Cassini UVIS Tracking Occultations and Ring Transparency Statistics. AGU Fall Meeting Abstracts 2017, P23B-2721.
- Estrada, P.R., Durisen, R.H., Cuzzi, J.N., Morgan, D.A., 2015. Combined structural and compositional evolution of planetary rings due to micrometeoroid impacts and ballistic transport. *Icarus* 252, 415–439.
- French, R.G., Nicholson, P.D., 2000. Saturn's rings II. Particle size inferred from stellar occultation data. *Icarus* 145, 502–523. <https://doi.org/10.1006/icar.2000.6357>.
- Fujiwara, A., Kamimoto, G., Tsukamoto, A., 1978. Expected shape distribution of asteroids obtained from laboratory impact experiments. *Nature* 272, 602–603. <https://doi.org/10.1038/272602a0>.
- Grainger, R.G., Lucas, J., Thomas, G.E., Ewan, G., 2004. The calculation of Mie derivatives. *Appl. Opt.* 43 (28), 5386–5393.
- Harbison, R.A., Nicholson, P.D., Hedman, M.M., 2013. The smallest particles in Saturn's A and C rings. *Icarus* 226, 1225–1240. <https://doi.org/10.1016/j.icarus.2013.08.015>.
- Hedman, M.M., Nicholson, P.D., 2013. Kronoseismology: using density waves in Saturn's C ring to probe the planets interior. *Astron. J.* 146 (12), 1–16. <https://doi.org/10.1088/0004-6256/146/1/12>.
- Hedman, M.M., Nicholson, P.D., 2014. More kronoseismology with Saturn's rings. *Mon. Not. R. Astron. Soc.* 444, 1369–1388.
- Hedman, M.M., Nicholson, P.D., 2019. Cassini Orbiter Saturn VIMS Ring Stellar Occultations 2.0, CO-SR-VIMS-4/5-OCC-V2.1, NASA Planetary Data System.
- Hedman, M.M., Nicholson, P.D., Salo, H., Wallis, B.D., Burratti, B.J., Baines, K.H., Brown, R.H., Clark, R.N., 2007. Self-gravity wake structures in Saturn's A ring revealed by Cassini-VIMS. *Astron. J.* 133 (6), 2624–2629.
- Hedman, M.M., Burt, J.A., Burns, J.A., Tiscareno, M.S., 2010. The shape and dynamics of a heliotropic dusty ringlet in the Cassini Division. *Icarus* 210 (1), 284–297. ISSN 0019-1035. <https://doi.org/10.1016/j.icarus.2010.06.017>.
- Jerousek, R.G., Colwell, J.E., Esposito, L.W., 2011. Morphology and variability of the Titan ringlet and Huygens ringlet edges. *Icarus* 216, 280–291.
- Jerousek, R.G., Colwell, J.E., Nicholson, P.D., Hedman, M.M., Esposito, L.W., 2016. Small particles and self-gravity wakes in Saturn's rings from UVIS and VIMS stellar occultations. *Icarus* 279, 36–50.
- Julian, W.H., Toomre, A., 1966. Non-axisymmetric responses of differentially rotating disks of stars. *Astrophys. J.* 146, 810–830.
- Kliore, A.J., Anderson, J.D., Armstrong, J.W., Asmar, S.W., Hamilton, C.L., Rappaport, N. J., Wahlquist, H.D., Ambrosini, R., Flasar, F.M., French, R.G., Jess, L., Marouf, E.A., Nagy, A.F., 2004. Cassini radio science. *Space Sci. Rev.* 115, 1–69.
- Lane, A.L., Hord, C.W., West, R.A., Esposito, L.W., Coffeen, D.L., Sato, M., Simmons, K.E., Pomphrey, R.B., Morris, R.B., 1982. Photopolarimetry from Voyager 2: preliminary results from Saturn, titan, and the rings. *Science* 215, 537–543. <https://doi.org/10.1126/science.215.4532.537>.
- Latter, Henrik N., Ogilvie, Gordon I., Choupeau, Marie, December 2012. The ballistic transport instability in Saturn's rings – I. Formalism and linear theory. *Monthly Notices of the Royal Astronomical Society* 427 (3), 2336–2348. <https://doi.org/10.1111/j.1365-2966.2012.22122.x>.
- Lewis, M.C., Stewart, G.R., 2009. Features around embedded moonlets in Saturn's rings: the role of self-gravity and particle size distributions. *Icarus* 199, 387–412.
- Marouf, E., 2019. Cassini Orbiter Saturn RSS Ring Radio Occultations 2.0, CO-SR-RSS-4/5-OCC-V2.0. NASA Planetary Data System.
- Marouf, Essam A., Tyler, G. Leonard, 1982. Microwave Edge Diffraction by Features in Saturn's Rings: Observations with Voyager 1. *Science*. 217 (4556), 243–245. <https://doi.org/10.1126/science.217.4556.243>.
- Marouf, E.A., Tyler, G.L., Zebker, H.A., Simpson, R.A., Eshleman, V.R., 1983. Particle size distributions in Saturn's rings from Voyager 1 radio occultation. *Icarus* 54, 189–211.

- Marouf, E.A., Tyler, G.L., Zebker, H.A., Rosen, P.A., 1986. Profiling Saturn's rings by radio occultation. *Icarus* 68, 120–166. [https://doi.org/10.1016/0019-1035\(86\)90078-3](https://doi.org/10.1016/0019-1035(86)90078-3).
- Matsui, T., Waza, T., Kani, K., and Suzuki, S. (1982), Laboratory simulation of planetesimal collision, *J. Geophys. Res.*, 87(B13), 10968–10982, doi:<https://doi.org/10.1029/JB087iB13p10968>.
- Nicholson, P.D., Hedman, M.M., 2010. Self-gravity wake parameters in Saturn's A and B rings. *Icarus* 206, 410–423 (doi:10/1016/j.icarus.2009.07.028).
- Pollack, J.B., 1975. *Space Science Reviews* 18, 3. <https://doi.org/10.1007/BF00350197>.
- Porco, C.C., West, R.A., Squyres, S., McEwen, A., Thomas, P., Murray, C.D., Del Genio, A., Ingersoll, A.P., Johnson, T.V., Neukum, G., Veverka, J., Dones, L., Brahic, A., Burns, J.A., Haemmerle, V., Knowles, B., Dawson, D., Roatsch, T., Beurle, K., Owen, W., 2004. Cassini imaging science: instrument characteristics and capabilities and anticipated scientific investigations at Saturn. *Space Sci. Rev.* 115, 363–497. <https://doi.org/10.1016/j.icarus.2016.06.012>.
- Showalter, M.R., Nicholson, P.D., 1990. Saturn's rings through a microscope: particle size constraints from the voyager PPS scan. *Icarus* 87, 285–306. <https://doi.org/10.1007/s11038-005-9060-8>.
- Spilker, L.J., Pilorz, S.H., Edgington, S.G., et al., 2005. *Earth Moon Planet* 96, 149. <https://doi.org/10.1007/s11038-005-9060-8>.
- Sremčević, Miodrag, Spahn, Frank, Duschl, Wolfgang J., December 2002. Density structures in perturbed thin cold discs. *Monthly Notices of the Royal Astronomical Society* 337 (3), 1139–1152. <https://doi.org/10.1046/j.1365-8711.2002.06011.x>.
- Tiscareno, M.S., Burns, J.A., Hedman, M.M., Porco, C.C., 2008. The population of propellers in Saturn's A ring. *Astron. J.* 135, 1083–1091.
- Tiscareno, M.S., Hedman, M.M., Burns, J.A., Weiss, J.W., Porco, C.C., 2013a. Probing the inner boundaries of Saturn's A ring with the Iapetus –1:0 nodal bending wave. *Icarus* 224, 201–208. <https://doi.org/10.1016/j.icarus.2013.02.026>.
- Tiscareno, M.S., Hedman, M.M., Burns, J.A., Castillo-Rogez, J., 2013b. Compositions and origins of outer planet systems: insights from the Roche critical density. *Astron. J.* 765, L28. <https://doi.org/10.1088/2041-8205/765/2/L28>.
- Tiscareno, M.S., Nicholson, P.D., Cuzzi, J.N., Spilker, L.J., Murray, C.M., Hedman, M.M., Colwell, J.E., Burns, J.A., Brooks, S.M., Clark, R.N., Cooper, N.J., Deau, E., Ferrari, C., Filacchione, G., Jerousek, R.G., Le Mouelic, S., Morishima, R., Pilorz, S., Rodriguez, S., Showalter, M.R., Badman, S.V., Baker, E.J., Burrati, B.J., Baines, K.H., Sotin, C., 2019. Close-range remote sensing of Saturn's rings during Cassini's ring grazing orbits and grand finale. *Science* 364 (6445), eaau1017. <https://doi.org/10.1126/science.aau1017>.
- Tyler, G.L., Marouf, E.A., Simpson, R.A., Zebker, H.A., Eshleman, V.R., 1983. The microwave opacity of Saturn's rings at wavelengths of 3.6 and 13 cm from voyager 1 radio occultation. *Icarus* 54, 160–188.
- Van de Hulst, H.C., 1957. *Light Scattering by Small Particles*. Dover Publications, Inc, N. Y, N.Y.
- Zebker, H.A., Marouf, E.A., Tyler, G.L., 1985. Saturn's rings: particle size distributions for thin layer model. *Icarus* 64, 531–548.
- Zhang, Z., Hayes, A.G., Janssen, M.A., Nicholson, P.D., Cuzzi, J.N., de Pater, I., Dunn, D. E., Estrada, P.R., Hedman, M.M., 2016. Cassini microwave observations provide clues to the origin of Saturn's C ring. *Icarus* 281, 297–321. <https://doi.org/10.1016/j.icarus.2016.07.0>.